Long COVID manifests with T cell dysregulation, inflammation, and an uncoordinated adaptive immune response to SARS-CoV-2

Kailin Yin[1,2*], Michael J. Peluso[3*], Xiaoyu Luo[1,2], Reuben Thomas[1], Min-Gyoung Shin[1], Jason Neidleman[1,2], Alicer Andrew[1,2], Kyrlia Young[1,2], Tongcui Ma[1,2], Rebecca Hoh[3], Khamal Anglin[3], Beatrice Huang[3], Urania Argueta[3], Monica Lopez[3], Daisy Valdivieso[3], Kofi Asare[3], Tyler-Marie Deveau[8], Sadie E. Munter[8], Rania Ibrahim,[3] Ludger Ständker[4], Scott Lu[5], Sarah A. Goldberg[5], Sulggi A. Lee[6], Kara L. Lynch[7], J. Daniel Kelly[5], Jeffrey N. Martin[5], Jan Münch[4], Steven G. Deeks[3], Timothy J. Henrich[8**], Nadia R. Roan[1,2**]

1. Gladstone Institutes, University of California, San Francisco, USA
2. Department of Urology, University of California, San Francisco, USA
3. Division of HIV, Infectious Diseases, and Global Medicine, University of California, San Francisco, USA
4. Core Facility Functional Peptidomics, Ulm University Medical Center, Meyerhofstrasse 1, Ulm, Germany
5. Department of Epidemiology and Biostatistics, University of California, San Francisco, USA
6. Zuckerberg San Francisco General Hospital and the University of California, San Francisco, USA
7. Division of Laboratory Medicine, University of California, San Francisco, USA
8. Division of Experimental Medicine, University of California, San Francisco, USA

*Equal Contribution
**Co-Corresponding

Abstract

Long COVID (LC), a type of post-acute sequelae of SARS-CoV-2 infection (PASC), occurs after at least 10% of SARS-CoV-2 infections, yet its etiology remains poorly understood. Here, we used multiple “omics” assays (CyTOF, RNAseq/scRNAseq, Olink) and serology to deeply characterize both global and SARS-CoV-2-specific immunity from blood of individuals with clear LC and non-LC clinical trajectories, 8 months following infection and prior to receipt of any SARS-CoV-2 vaccine. Our analysis focused on deep phenotyping of T cells, which play important roles in immunity against SARS-CoV-2 yet may also contribute to COVID-19 pathogenesis. Our findings demonstrate that individuals with LC exhibit systemic inflammation and immune dysregulation. This is evidenced by global differences in T cell subset distribution in ways that imply ongoing immune responses, as well as by sex-specific perturbations in cytolytic subsets. Individuals with LC harbored increased frequencies of CD4+ T cells poised to migrate to inflamed tissues, and exhausted SARS-CoV-2-specific CD8+ T cells. They also harbored significantly higher levels of SARS-CoV-2 antibodies, and in contrast to non-LC individuals, exhibited a mis-coordination between their SARS-CoV-2-specific T and B cell responses. RNAseq/scRNAseq and Olink analyses similarly revealed immune dysregulatory mechanisms, along with non-immune associated perturbations, in individuals with LC. Collectively, our data suggest that proper crosstalk between the humoral and cellular arms of adaptive immunity has broken down in LC, and that this, perhaps in the context of persistent virus, leads to the immune dysregulation, inflammation, and clinical symptoms associated with this debilitating condition.

Introduction

Intense efforts are underway to determine the pathophysiology of post-acute sequelae of SARS-CoV-2 infection (PASC), a set of conditions affecting at least 10% of individuals recovering from COVID-19 [1, 2, 3]. PASC, which includes the unexplained, debilitating symptoms that characterize LC, remains a major public health challenge despite the availability of SARS-CoV-2 vaccination and treatment [4, 5, 6, 7, 8]. Although the underlying cause or causes of LC are incompletely understood, multiple mechanisms including microvascular dysregulation [9, 10], autoimmune phenomena [11, 12, 13], and reactivation of latent human herpesviruses [12, 14, 15] have been proposed as contributors to inflammatory responses, particularly in tissues, which could in turn drive symptoms that individuals experience. In addition, persistence of SARS-CoV-2 antigen can occur months after infection [16], and has recently been demonstrated in a subset of immunocompetent individuals with LC [17, 18, 19]. However, there are currently no accepted therapies for LC, in part due to limited insight into the underlying mechanisms of the condition to date [2].

To try to better understand the molecular underpinnings of LC, multiple "omics"-based approaches have recently been implemented on plasma specimens. Such studies have revealed individuals with LC to more often have elevated levels of inflammatory cytokines such as IFNβ and IL8, but low levels of cortisol [12, 20, 21]. These results are consistent with the ongoing immunologic perturbations that have been consistently observed in individuals experiencing LC [12, 21, 22, 23, 24, 25, 26]. Serological analyses have also found the presence of auto-antibodies during the acute or post-acute phases of infection to be associated with LC [11, 12, 13], although this has not been observed consistently [20, 27, 28]. Indeed, recent proteome-wide autoantibody analysis by PhIP-Seq revealed a clear autoreactivity signature associated with prior COVID-19, but no unique autoreactivity signature comparing people with and without LC [28]. Intriguingly, a subset of auto-antibodies against chemokines have even been reported recently to associate with protection against LC [29]. Elevated levels of SARS-CoV-2 antibodies have also been associated with LC [20]. "Omics" analyses of immune cells in the form single-cell transcriptomics on PBMCs have likewise been performed, resulting in the classification of LC into multiple endotypes, and uncovering the persistent elevation of select immune subsets – including myeloid and NK subsets – in some phenotypes of LC [12]. This study, however, did not examine individuals whose symptoms persisted beyond three months, and did not examine LC resulting from initial mild-to-moderate (non-hospitalized) cases of COVID-19, which comprise the vast majority of those experiencing this condition.

T cells play an important role in SARS-CoV-2 immunity and pathogenesis, yet relatively little is known about their role in LC. A limited set of studies that have examined SARS-CoV-2-specific T cell responses have implicated these cells in LC, albeit with conflicting results. While some studies have found elevated SARS-CoV-2-specific T cell responses in LC as compared to non-LC individuals [26, 30], we have observed faster decay of subsets of SARS-CoV-2-specific CD8+ T cells in the context of LC [31]. Apart from a transcriptomic/CITE-seq analysis of SARS-CoV-2-specific CD8+ T cells by MIRA, which identified unique features associated with LC two to three months after COVID-19 hospitalization [12], in-depth analyses of the phenotypic and functional features of SARS-CoV-2-specific T cells from individuals with LC are lacking. In particular, the profile of CD4+ T cells, key orchestrators of adaptive immunity, in individuals with LC is currently unknown.

We have previously used deep phenotypic characterization of SARS-CoV-2-specific T cells by CyTOF to identify differentiation states, effector functions, and/or homing properties of SARS-CoV-2-specific T cells associated with long-lived memory responses, fatal COVID-19, vaccination, and hybrid immunity [32, 33, 34, 35], and to characterize pulmonary T cell responses in a mouse model of severe COVID-19 [36]. As these insights into COVID-19 immunity and pathogenesis were obtained using these next-generation T cell characterization assays in ways

that would not have been captured using solely more traditional T cell assays, we reasoned that a similar in-depth analysis could identify T cells that protect or contribute to the symptoms of LC.

Therefore, in this study we deeply characterized T cell immunity during the post-acute phase of infection by CyTOF. We then combined these data with standard serological analyses, as well as additional "omics" techniques: RNAseq/scRNAseq, and high-dimensional plasma proteomics using the Olink Explore Proximity Extension Assay (PEA), the latter of which enables simultaneous quantitation of 384 analytes from plasma. We leveraged a cohort of LC and non-LC individuals with detailed longitudinal characterization and biospecimen collection prior to SARS-CoV-2 vaccination or reinfection, which could confound interpretation of SARS-CoV-2-specific T cell and antibody responses, to identify clues to the immunologic processes that might drive LC. By performing this holistic, integrative analysis on a well-matched set of LC and non-LC individuals with consistent phenotypes for 8 months after infection, we were able to identify unique immune features associated with LC that inform on the mechanistic underpinnings of this debilitating disease.

Results

LC and non-LC participants

To study the phenotypes and effector functions of immune cells from individuals experiencing Long COVID-19 symptoms, we analyzed blood samples from 27 LC and 16 non-LC individuals from the San Francisco-based Long-term Impact of Infection with Novel Coronavirus (LIINC) cohort (NCT04362150) [37]. Specimens were collected 8 months following infection, but individuals had been followed since at least 4 months post-infection to characterize LC over time. Individuals with LC were defined as those that consistently met the case definition for LC (at least one COVID-19-attributed symptom that was new or worsened since the time of SARS-CoV-2 infection, and was at least somewhat bothersome) at both 4 and 8 months, while clinically matched non-LC individuals did not experience any lingering symptoms for the entire 8 months after SARS-CoV-2 infection. Importantly, at the time of specimen collection (in 2020-2021), none of the participants had yet received a SARS-CoV-2 vaccine, which would confound the SARS-CoV-2-specific serological and T cell analyses (Fig. S1A).

Overall, the enrolled individuals had a median age of 46 years (range 19 to 71) and 58.1% identified as White (Table 1, Table 2, Table S1). Individuals with LC were more likely to be female (63% vs 44%) (Fig. S1B) and included those previously hospitalized during the acute phase of COVID-19 (26% vs 13%) (Fig. S1C). The individuals with LC analyzed herein were all highly symptomatic, and consistently exhibited LC symptoms over an 8-month period (Fig. S1D). Although the overall population was relatively healthy with few pre-existing comorbidities, when present these tended to be more common in the LC group (Fig. S1E), consistent with the current understanding that certain comorbid conditions such as obesity, diabetes, and pre-existing lung disease are likely to be risk factors for LC. This is also consistent with our observation that in our cohort, individuals with LC had higher BMI than those without LC (Fig. S1F).

Experimental design

SARS-CoV-2 serological analysis and five "omics" assays were performed on the same blood specimens from our cohort of LC and non-LC individuals (Fig. 1). Plasma/sera were analyzed for RBD-specific antibody levels, and for the levels of 394 analytes using the Olink platform. PBMCs from the same specimens were subjected to bulk and single-cell RNAseq (scRNAseq), as well as in-depth CD4+ and CD8+ T cell phenotyping using a 39-parameter CyTOF panel designed to simultaneously interrogate the differentiation states, activation states, effector functions, and homing properties of T cells (Table S2). Cells were phenotyped by CyTOF at baseline and following a 6-hour stimulation with SARS-CoV-2 peptides to identify and characterize SARS-CoV-2-specific T cells at the single-cell level through intracellular cytokine staining. The

RNAseq/scRNAseq and Olink datasets, as well as the CyTOF datasets corresponding to total and SARS-CoV-2-specific T cells, were visualized and analyzed using a variety of integrative high-dimensional analysis approaches (Fig. 1). In total, we obtained 6 distinct datasets, enabling us to assess humoral response (serology), plasma analytes (Olink), transcriptional signatures at the bulk (RNAseq) and single-cell (scRNAseq) levels, T cell features (CyTOF), and SARS-CoV-2-specific T cell phenotypes and effector functions (CyTOF).

SARS-CoV-2-specific T cells exhibit similar frequencies and effector profiles in LC and non-LC individuals

To quantitate total and SARS-CoV-2-specific T cells, normalized events from the CyTOF datasets were gated on intact, live, singlet events, followed by gating for CD4+ and CD8+ T cells (Fig. S2A, B). The T cells were assessed for expression of all our panel's effector molecules, which were chosen because of their roles in T-cell immunity and pathogenesis. These consisted of the cytokines IFNγ, TNFα, IL2, IL4, IL6, IL17, and MIP1β, and cytolytic markers including granzyme B and perforin (Fig. S2C, D). To determine which T cells were SARS-CoV-2-specific, we established a stringent set of rules based on the frequencies of cells expressing these effectors in samples treated or not with SARS-CoV-2 peptides (details in Methods). This analysis revealed that a combination of IFNγ, TNFα, and/or IL2 specifically identified the vast majority of SARS-CoV-2-specific CD4+ T cells (Fig. 2A, S2C), while a combination of IFNγ, TNFα, and/or MIP1β specifically identified the vast majority of SARS-CoV-2-specific CD8+ T cells (Fig. 2B, S2D).

Using Boolean gating, we then compared the frequencies of SARS-CoV-2-specific T cells between LC and non-LC individuals. No significant differences were observed when looking at the total population of SARS-CoV-2-specific T cells (expressing any combination of IFNγ, TNFα, IL2, and/or MIP1β) (Fig. 2C, D), or when looking at SARS-CoV-2-specific T cells producing any of the individual effector cytokines (Fig. S3A, B).

To quantitate polyfunctional cells, we implemented Simulation Program with Integrated Circuit Emphasis (SPICE) analyses. Overall, the distribution of polyfunctional SARS-CoV-2-specific T cells was similar between the LC and non-LC individuals, among both the CD4+ and CD8+ T cell compartments (Fig. 2E, F). The most polyfunctional T cells (IFNγ+TNFα+IL2+ for SARS-CoV-2-specific CD4+ T cells, and IFNγ+TNFα+MIP1β+ for SARS-CoV-2-specific CD8+ T cells) tended to be more abundant in non-LC individuals, but this trend did not reach statistical significance (Fig. 2E, F). TNFα single-positive cells made up the majority of SARS-CoV-2-specific T cells in both LC and non-LC individuals, particularly among CD4+ T cells where >50% of the responding cells singly produced this effector cytokine (Fig. 2E, F). By contrast, SARS-CoV-2-specific CD8+ T cells more frequently produced IFNγ than SARS-CoV-2-specific CD4+ T cells, independent of LC status (Fig. 2E, F). Overall, these analyses suggest that SARS-CoV-2-specific T cells have similar effector profiles in LC and non-LC individuals. However, one interesting exception was found in that IL6 was found to be induced within CD4+ T cells after SARS-CoV-2 peptide stimulation (Fig. S3C) exclusively among individuals with LC, albeit only in a small subset of these people (14%) (Fig. S3D).

Individuals with LC exhibit different distributions of T cell subsets including in sex-dimorphic fashion

T cells can be classified not only by the effector molecules they produce, but also by T cell lineage markers. We next took advantage of the deep phenotyping capabilities of CyTOF to compare classical subset distributions among total and SARS-CoV-2-specific T cells. Naïve T cells (Tn), stem cell memory cells (Tscm), central memory T cells (Tcm), effector memory T cells (Tem), transitional memory cells (Ttm), and effector memory RA (Temra) cells were identified from both CD4+ and CD8+ T cells through sequential gating strategies (Fig. S4A, B). In addition, T follicular helper cells (Tfh) and regulatory T cells (Treg) were identified from the CD4+ compartment (Fig. S4A). Among total CD4+ T cells, the Tcm, Tfh, and Treg subsets were all

199 significantly elevated among the individuals with LC (Fig. 3A). The other CD4+ T cell subsets
200 were not different between the LC and non-LC groups, and among SARS-CoV-2-specific CD4+
201 T cells none of the subsets were significantly different (Fig. 3A, B). Among both total and SARS-
202 CoV-2-specific CD8+ T cells, no subsets were statistically different between the LC and non-LC
203 groups; however, there was a trend (p=0.09) for the Tem subset to be higher among total CD8+
204 T cells in the LC group (Fig. S5).
205 To examine T cell distribution between LC and non-LC individuals using not only the T cell
206 lineage markers, but all the phenotyping and effector markers analyzed in our CyTOF panel, we
207 examined the mean expression levels of all these markers among both total and SARS-CoV-2-
208 specific T cells. Following multiple correction adjustment, no antigens were significantly
209 differentially expressed between the individuals with or without LC (Fig. S6-S9). As excess
210 inflammation has been implicated in the context of both severe COVID-19 and LC, we additionally
211 performed manual gating to assess for evidence of increased T cell activation in individuals with
212 LC. This revealed no significant differences in the percentages of cells expressing acute activation
213 markers CD38, HLADR, and Ki67 between individuals with and without LC (Fig. S10). T cells
214 expressing all three activation markers were also not differentially represented among the two
215 groups of individuals (Fig. S10). To analyze the complexity of our high-dimensional datasets in
216 ways not captured through such one-dimensional analyses of individual marker expression, we
217 performed clustering analyses. CD4+ and CD8+ T cells fell into six (Clusters A1-A6) and five
218 (Clusters B1-B5) clusters, respectively (Fig. S11A, S12A), that did not differ significantly between
219 the LC and non-LC groups, except when we stratified the participants by sex. Among CD4+ T
220 cells, cluster A1 was significantly over-represented in LC than non-LC females (but not males),
221 while cluster A4 was significantly over-represented in LC than non-LC males (but not females)
222 (Fig. S11B). Cluster A1 was composed of naïve CD4+ T cells, and expressed low levels of
223 activation markers and inflammatory tissue homing receptors, and high levels of the lymph node
224 homing receptors (Fig. S11C). By contrast, cluster A4 was composed of terminally differentiated
225 effector memory CD4+ T cells and expressed high levels of receptors associated with homing to
226 inflamed tissues but not those associated with homing to lymph nodes (Fig. S11D). They also
227 expressed elevated levels of the cytolytic markers including perforin and granzyme B (Fig. S11D).
228 Among CD8+ T cells, cluster B1 was significantly under-represented in LC while cluster B2 was
229 significantly over-represented, but only among females (Fig. S12B). Interestingly, the phenotypic
230 features of cluster B1 mirrored those of cluster A1, while the features of cluster B2 mirrored those
231 of cluster A4 (Fig. S12 C, D). These observations, together with the observation that cluster A4
232 trended higher in the female LC group, suggest that female individuals with LC harbor relatively
233 low frequencies of resting naïve T cells expressing low levels of inflammatory tissue-homing
234 receptors, and high frequencies of terminally differentiated effector memory T cells expressing
235 inflammatory tissue homing receptors and cytolytic markers; this was true among both CD4+ and
236 CD8+ T cells. More broadly, the results suggest that there are sex-dimorphic differences in the
237 subset distribution of T cells between LC and non-LC individuals.
238
239 ***Preferential expression of some tissue-homing receptors on CD4+ T cells from individuals***
240 ***with LC***
241 We then focused on the phenotypic features of SARS-CoV-2-specific T cells. Although
242 clustering analyses did not reveal significant differences between the LC vs. non-LC groups (not
243 shown), contour-based tSNE visualization revealed that the cells from the LC vs. non-LC groups
244 tended to concentrate in different areas suggesting some phenotypic differences (Fig. 4A, 5A).
245 Focusing first on the SARS-CoV-2-specific CD4+ T cells, we found that the chemokine receptors
246 CXCR4, CXCR5, and CCR6 were all expressed at higher levels in the cells from the LC as
247 compared to the non-LC individuals (Fig. 4B). Gating on SARS-CoV-2-specific CD4+ T cells co-
248 expressing various pairs of these chemokine receptors revealed that those that were
249 CXCR4+CXCR5+ and CXCR5+CCR6+ were significantly increased, while those that were

250 CXCR4+CCR6+ trended higher, in individuals with LC (Fig. 4C). Interestingly, this same pattern
251 was observed among total CD4+ T cells (Fig. 4D), in a manner confirmed by FACS (FACS-based
252 assessment of receptor expression significantly associated with measurements made by CyTOF,
253 Fig. S13A), but now where the elevated frequencies of CXCR4+CCR6+ CD4+ T cells in LC also
254 reached statistical significance (Fig. S13B, C). These results together suggest that expression of
255 tissue-homing receptors is elevated in CD4+ T cells – including but also beyond those with
256 specificity for SARS-CoV-2 – in individuals with LC.
257 It was intriguing to us that CXCR5 was a common marker among the CXCR4+CXCR5+,
258 CXCR5+CCR6+, and Tfh CD4+ T cell subsets, both of which were found to be significantly
259 elevated in LC (Fig. 4, S13). This prompted us to examine whether there was an association
260 between the frequencies of Tfh and these other chemokine receptor-expressing subsets.
261 Intriguingly, we observed significant associations between the frequencies of Tfh and these
262 subsets, particularly for the LC group (Fig. 4E). When we performed this correlation analysis
263 among SARS-CoV-2-specific instead of total CD4+ T cells, significant positive associations were
264 observed only among the LC group, while in the non-LC group there was a negative association
265 trend (Fig. 4F).
266
267 ***SARS-CoV-2-specific CD8+ T cells from individuals with LC preferentially co-express the***
268 ***checkpoint molecules PD1 and CTLA4***
269 A similar manual inspection of CD8+ T cell data revealed the checkpoint/exhaustion
270 markers PD1 and CTLA4 to be expressed at elevated levels on SARS-CoV-2-specific CD8+ T
271 cells from the LC as compared to non-LC individuals, while the exhaustion marker TIGIT was not
272 differentially expressed (Fig. 5B). Consistent with these data, SARS-CoV-2-specific CD8+ T cells
273 that were PD1+CTLA4+, but not those that were TIGIT+CTLA4+ or PD1+TIGIT+, were
274 significantly elevated in individuals with LC (Fig. 5C). Interestingly, however, frequencies of total
275 PD1+CTLA4+ CD8+ T cells were not different between the LC and non-LC individuals (Fig. 5D).
276 These results were confirmed by FACS analyses of the same patient specimens (Fig. S14).
277 Although PD1 and CTLA4 are also activation markers, the fact that we didn't see elevation of
278 acute activation markers CD38, HLADR, or Ki67 on SARS-CoV-2-specific CD8+ T cells from
279 individuals with LC (Fig. S10) suggests that what is being observed is not simply elevated T cell
280 activation. These results together suggest that LC-derived CD8+ T cells recognizing SARS-CoV-
281 2 uniquely exhibit phenotypic features of exhaustion (but not acute activation), as reflected by co-
282 expression of PD1 and CTLA4, perhaps due to persistence of SARS-CoV-2 antigen that cannot
283 be eliminated in individuals with LC.
284
285 ***Individuals with LC exhibit a mis-coordinated T and antibody response***
286 Serological analysis revealed significantly higher SARS-CoV-2 RBD antibody levels in the
287 LC group than in the non-LC group (Fig. 6A). Interestingly, the two individuals with LC with the
288 highest antibody levels (green oval) were not those that had the highest frequencies of exhausted
289 (PD1+CTLA4+) SARS-CoV-2-specific CD8+ T cells (purple oval) (Fig. 6B), even though both
290 features are consistent with a persistent SARS-CoV-2 reservoir. Interestingly, however, the
291 individuals with the highest frequencies of exhausted SARS-CoV-2-specific CD8+ T cells did have
292 the lowest frequencies of SARS-CoV-2-specific CD4+ Treg cells, and the frequencies of these
293 two subsets of cells negatively correlated in LC but not non-LC individuals (Fig. 6C). When we
294 assessed the association between antibody levels and SARS-CoV-2-specific T cell frequencies,
295 we found a significant ($p=0.0418$ for CD4, $p=0.0007$ for CD8) positive correlation, but only in the
296 non-LC individuals (Fig. 6D, F). The frequencies of SARS-CoV-2-specific Tfh cells also
297 significantly ($p=0.0014$) positively correlated with antibody responses in non-LC individuals but
298 not in individuals with LC (Fig. 6E). These results suggest that a mis-coordinated humoral and
299 cell-mediated response, previously implicated in severe COVID-19 [38], may also be a hallmark of
300 LC.

301
302 ***Individuals with LC exhibit global alterations in PBMCs reflecting immune and non-***
303 ***immune dysregulation***
304 To determine whether the differences between LC and non-LC individuals extended
305 beyond T cells and the humoral response, we examined the transcriptome of the PBMCs.
306 Assessing for total changes in gene expression in PBMCs by bulk RNAseq, we found only two
307 genes that remained significantly differentially expressed after multiple comparison adjustments:
308 OR7D2 (Olfactory Receptor 7D2) and ALAS2 (5'-Aminolevulinate Synthase 2), both of which were
309 over-expressed in the individuals with LC (Fig. 7A). Interestingly, this was observed in a non-
310 overlapping manner in that the four individuals with highest OR7D2 expression did not overlap
311 with the four individuals with highest ALAS2 expression. OR7D2 encodes a G-protein-coupled
312 receptor that responds to odorant molecules in the nose, while ALAS2 encodes a protein that
313 catalyzes the first step in heme synthesis, defects in which can lead to anemia.
314 Further analysis of the RNAseq datasets revealed that a number of genes other than
315 OR7D2 and ALAS2 were upregulated in individuals with LC, although not significantly so after
316 conservative adjustments for multiple comparisons; these included a module of genes that
317 regulate heme synthesis and carbon dioxide transport (ALAS2, HBB, CA1, HBA1, SLC4A1, HBD,
318 HBA2) (Fig. 7B, S15A). By contrast, a module consisting of immunoglobin kappa, lambda, and
319 heavy chain genes, along with BIRC5, which plays an important role in T cell survival and function
320 [39], were more highly expressed in non-LC individuals (Fig. 7B, S15A). Gene ontology analysis
321 revealed that genes from both of these modules were highly networked together (Fig. 7C),
322 strongly suggesting that these genes are indeed linked to LC.
323 In order to determine which subsets of cells were expressing our top differentially
324 expressed genes (DEGs) OR7D2 and ALAS2, as well as to gain a more granular view of the
325 transcriptional features of cells from individuals with LC, we selected a subset of the participants
326 for further analyses by scRNAseq. Intriguingly, females were vastly over-represented among the
327 LC individuals expressing high levels of OR7D2 or ALAS2: the top five OR7D2 expressors were
328 all female, and among the top six ALAS2 expressors, five were female (the third highest ALAS2
329 expressor was male). To avoid sex-associated confounders, we limited our scRNAseq studies to
330 female donors. We selected the four LC females with the highest OR7D2 expression and the four
331 LC females with the highest ALAS2 expression (purple asterisks in Fig. 7A), and four randomly
332 selected non-LC females for comparison. Integrative analysis of all 12 donors identified 11
333 clusters of cells, including subsets of CD4+ T cells, CD8+ T cells, B cells, monocytes, and innate-
334 like cells (Fig. 7D). In addition, small numbers of granulocytes and platelets were identified; their
335 low numbers were expected as PBMCs and not whole blood were analyzed. While the major
336 clusters did not differ in frequency between the LC and non-LC groups, the granulocyte cluster
337 was significantly less abundant ($p=0.006$) while the platelet cluster was significantly more
338 abundant ($p=0.01$) in individuals with LC. Consistent with lack of major perturbations at the
339 transcriptional level, visualization of the datasets by LC vs. non-LC status (Fig. S16A), and by the
340 two groups of LC (OR7D2^{high} and ALAS2^{high}) (Fig. S16B), did not reveal profound differences.
341 Consistent with the bulk RNAseq data, OR7D2 was expressed at the highest levels in the
342 OR7D2^{high} LC cells, and ALAS2 was expressed at the highest levels in the ALAS2^{high} LC cells
343 (Fig. S16C). When we assessed which clusters of cells expressed OR7D2 and ALAS2, we found
344 that these transcripts were broadly expressed in all subsets except the granulocyte and platelet
345 clusters (Fig. 7E, S16D), with the caveat that the low numbers of cells in the latter two clusters
346 likely precluded ability to detect these transcripts. Interestingly, among clusters expressing
347 OR7D2 or ALAS2, only a small fraction of cells (<0.5%) expressed these genes (Fig. S16D),
348 suggesting that small numbers of cells harboring high levels of OR7D2/ALAS2 were responsible
349 for the original identification of these DEGs from the bulk RNAseq analysis. Clusters expressing
350 OR7D2 generally expressed this gene at the highest levels in the OR7D2^{high} LC group (Fig. S16E).
351 Similarly, clusters expressing ALAS2 generally expressed this gene at the highest levels in the

352 ALAS2^{high} LC group (Fig. S16F). Interrogating cluster-specific gene expression beyond just
353 OR7D2 and ALAS2 expression revealed only 3 genes as significantly differentially expressed
354 between the LC and non-LC groups, two within a CD4+ T cell cluster and one within the monocyte
355 cluster (Table S3). Notably, however, using a less stringent cutoff of $p<0.1$, we found that the
356 activation marker GITR was more highly expressed ($p=0.07$) in a cluster of CD4+ T cells from the
357 individuals without LC. Reasoning that LC is heterogeneous and that the OR7D2^{high} and ALAS2^{high}
358 groups may represent different subtypes of individuals with LC, we then compared these groups
359 individually with our non-LC controls. This revealed 35 DEGs in the OR7D2^{high} group (Table S4),
360 and 14 DEGs in the ALAS2^{high} group ($p<0.05$) (Table S5). With a less stringent cutoff of $p<0.1$, a
361 number of additional immune-related genes of interest were additionally identified, including
362 downregulation of the Th17 lineage marker RORC ($p=0.06$) and upregulation of immune
363 checkpoint KLRG1 ($p=0.08$) in subsets of CD4+ T cells from the OR7D2^{high} LC as compared to
364 non-LC individuals. Overall, our scRNAseq results support immune dysregulation in LC, and
365 validate the OR7D2 and ALAS2 bulk RNAseq data.
366
367 ***Individuals with LC exhibit global alterations in sera reflecting immune dysregulation and***
368 ***inflammation***
369 Finally, we implemented Olink analysis to characterize the proteome of the sera from our
370 participant specimens. This also revealed global changes associated with LC, including a module
371 consisting of elevated levels of proteins associated with inflammation (LGALS9, CCL21, CCL22,
372 TNF, CXCL10, CD48) (Fig. 7F, S15B). Proteins associated with immune regulation (IL1RN, CD22)
373 were also elevated in individuals with LC (Fig. 7F, S15B). Interestingly, although IL4 and IL5 are
374 both canonical cytokines for Th2 responses, these two cytokines exhibited very different
375 expression patterns (Fig. 7F, S15B), and individuals with LC overall exhibited elevated levels of
376 IL4 yet lower levels of IL5 (Fig. 7G). CCL22, a ligand for the Th2 marker CCR4, was expressed
377 at elevated levels in individuals with LC (Fig. 7G). Together, these results suggest an elevated
378 yet mis-coordinated Th2 response (elevated IL4 and CCL22 but diminished IL5) in individuals
379 with LC. Intriguingly, IL4, but not IL5 or CCL22, significantly positively associated with the
380 percentages of CXCR4+CXCR5+ and CXCR5+CCR6+ CD4+ T cells (more frequent in LC, Fig.
381 4), but only in the individuals with LC (Fig. S17). By contrast, individuals without LC exhibited a
382 significant negative association (Fig. S17). As for the RNAseq data, networking of genes from
383 the inflammatory and immunoregulatory modules, as well as from the Th2 markers IL4, IL5, and
384 CCL22, suggests a biologically-relevant plausible association of all of these genes with LC.
385 Overall, our findings suggest that LC is associated with unique, and likely complex, global immune
386 dysregulation.
387
388 **Discussion**
389 Using multiple "omics" analytical approaches on specimens from individuals exhibiting
390 consistent LC trajectories, we demonstrate that individuals with LC exhibit perturbations in both
391 total and SARS-CoV-2-specific T cells, which manifests at a global level as mis-coordination
392 between the two main arms of adaptive immunity and overall changes in gene expression. In
393 this analysis, we took care to limit several confounders that often constrain studies of LC. First,
394 we carefully selected a cohort of individuals who consistently met the case definition for LC over
395 an 8-month period and compared them with individuals who, when measured in the same way,
396 using the same study instruments at the same timepoints, consistently demonstrated complete
397 recovery. Second, to avoid surveillance bias, all assays were applied on samples from the same
398 timepoint (8 months post-COVID), and we chose this relatively late timepoint so that we would
399 not be confounded by individuals only exhibiting shorter-term LC (e.g., which resolve
400 spontaneously after 4-6 months). Third, we restricted our analysis to only those individuals who
401 prior to the time of sampling had not yet received a SARS-CoV-2 vaccine and who had not had

402 a known or suspected SARS-CoV-2 re-infection, as either could markedly affect our SARS-
403 CoV-2-specific antibody and T cell measurements.
404 Our CyTOF data revealed profound changes in classical subset distribution among total
405 CD4+ T cells in individuals with LC, specifically a significantly higher proportion of CD4+ Tcm,
406 Tfh, and Treg cells. Elevated frequencies of Tcm in LC have been reported previously [30],
407 although another group reported the opposite observation that Tcm frequencies were decreased
408 in LC [20]. The reason for these discrepancies is not clear, but may reflect the composition of the
409 clinical cohorts studied: while our study and the other one which also reported elevated Tcm
410 cells examined only non-vaccinated individuals, the study where Tcm were decreased included
411 some individuals who received a SARS-CoV-2 vaccine prior to sampling. Higher frequencies of
412 Tfh and Treg cells in individuals with LC have, to our knowledge, not been previously reported.
413 Interestingly, however, a prior study reported that elevated frequencies of activated Treg cells
414 during acute SARS-CoV-2 infection predicted development of LC two to three months later [12],
415 which together with our findings is consistent with Tregs being involved in both LC initiation and
416 maintenance.
417 Elevated frequencies of Tcm, Tfh, and Treg in individuals with LC indicate an ongoing
418 immune response persisting at 8 months post-infection. This immune response, however, may
419 not necessarily be directed against SARS-CoV-2, and could potentially be directed against other
420 viruses (*e.g.,* reactivated EBV or other herpes viruses) or auto-antigens [12]. Indeed, we did not
421 find significantly higher magnitude of the SARS-CoV-2-specific T cell response as determined
422 by intracellular cytokine staining in individuals with LC, consistent with prior observations
423 reported from the activation-induced marker (AIM) assay [30]. We also did not find individuals with
424 LC to harbor more polyfunctional SARS-CoV-2-specific T cells, and in fact polyfunctionality
425 trended lower in both the CD4 and CD8 compartments. At the same time, other studies have
426 reported higher [26] or lower [31] SARS-CoV-2-specific T cell responses in the context of LC.
427 Discrepancies may stem from differences in the LC cohorts analyzed, and in the assays used to
428 quantitate T cell responses (including the SARS-CoV-2 proteins examined, and the approaches
429 used to identify responding cells). We note that our approach was comprehensive in that we
430 monitored expression levels of 10 different effectors, and settled on a subset of five of these
431 (IFNγ, TNFα, IL2, MIP1β, IL6) using strict criteria, to define SARS-CoV-2-specific T cells.
432 One aspect highly consistent between all studies to date is the ability to detect SARS-
433 CoV-2-specific T cells in both LC and non-LC individuals, months after infection. This could
434 simply be attributed to the long-term persistence of memory T cells elicited by SARS-CoV-2, but
435 may also indicate the persistence of a long-lived tissue viral reservoir as has been documented
436 [16]. Indeed, we found that in LC relative to non-LC individuals, SARS-CoV-2-specific CD8+ T
437 cells, but not total CD8+ T cells, more frequently expressed the exhaustion markers PD1 and
438 CTLA4, which is consistent with ongoing stimulation with viral antigens. Also in support of a
439 potential persistent reservoir is our observation of higher SARS-CoV-2 antibody levels in LC as
440 compared to non-LC individuals, which has also been previously seen with Spike-specific IgG
441 levels [30]. Interestingly, our data revealed that the individuals with the highest frequencies of
442 SARS-CoV-2-specific CD8+ T cells co-expressing the exhaustion markers PD1 and CTLA4
443 were not those with the highest SARS-CoV-2 antibody levels, suggesting that there may be
444 multiple endotypes of LC being driven by persisting virus. Consistent with this possibility, a
445 recent RNAseq study identified two types of LC: one being driven by high expression of Ig-
446 related genes, and the other being associated with low levels of Ig-related genes [40]. Based on
447 these observations as well as case reports of improvement in LC symptoms following antiviral
448 treatment [41, 42, 43], nirmatrelvir-ritonavir treatment as an antiviral strategy to clear this putative
449 LC-associated SARS-CoV-2 reservoir is underway (NCT05576662, NCT05595369,
450 NCT05668091). Future studies could evaluate other antivirals or monoclonal antibodies, and in
451 light of our PD1 and CTLA4 expression data might consider incorporating checkpoint inhibition
452 in conjunction with antivirals to reinvigorate T cells' ability to help eliminate residual viremia.

453 One intriguing aspect of LC that emerged from our study is sex-dimorphism in T cell
454 phenotypes. This perhaps is not so surprising given the different trajectories of COVID-19
455 between males and females [44] and the observation that LC is more common in females [5, 45]. Our
456 data revealed that, among females, a subset of activated and cytotoxic T cells was more
457 elevated in LC than in non-LC individuals; intriguingly, the opposite pattern was observed in
458 males. The presence of cytotoxic T cells has been associated with gastrointestinal LC
459 symptoms [12] and it will be of interest in future studies to establish whether biological sex impacts
460 LC-associated cytotoxic T cell function. We also found in our RNAseq analysis that individuals
461 expressing the highest levels of the top LC-associated DEGs (OR7D2 and ALAS2) were heavily
462 biased towards female sex, again emphasizing the sex dimorphism of LC. Intriguingly, biological
463 sex was recently shown to manifest in the context of differential responses to influenza vaccines
464 after COVID-19 convalescence [46], although individuals with LC were not examined therein.
465 While SARS-CoV-2-specific CD8+ T cells from individuals with LC showed phenotypic
466 features of exhaustion, their CD4+ counterparts preferentially expressed the tissue-homing
467 receptors CXCR4, CXCR5, and CCR6. Of note, these receptors can all direct immune cells to
468 the lung, and CXCR4 is of particular interest as its expression on bystander T cells has been
469 associated with severe/fatal COVID-19 [34]. Elevated expression of CXCR4 was also observed on
470 pulmonary neutrophils from severe COVID-19 cases, suggesting it as a potential target for
471 constraining ARDS induced by SARS-CoV-2 infection [47]. It has also recently been observed to
472 be elevated on pulmonary immune cells in the context of post-acute sequelae following SARS-
473 CoV-2 infection of mice [48]. As we found elevated expression of CXCR4 not only on SARS-CoV-
474 2-specific but also total CD4+ T cells in the context of LC, targeting of this receptor as well as
475 other chemokine receptors may be useful to limit immune cell infiltration into the lung, which
476 may persist in an elevated state of inflammation in individuals with LC. Intriguingly, targeting of
477 chemokine-mediated signaling has also been recently suggested as a therapy for LC based on
478 observations that auto-antibodies against a variety of chemokines associate with protection from
479 LC [29].
480 Another intriguing observation we made about the SARS-CoV-2-specific CD4+ T cells
481 from individuals with LC is their production of IL6 in response to spike peptide stimulation.
482 Although this was observed in only a small minority of individuals with LC, it suggests that a
483 highly inflammatory response directed against the virus, persisting for at least 8 months post-
484 infection, could be a driver of the sequelae. Although IL6 is not typically produced by
485 lymphocytes, such atypical production of IL6 by T cells has been observed in the context of
486 severe COVID-19 [34] and by B cells in the context of HIV pathogenesis [49]. Interestingly, elevated
487 IL6 levels have been associated with pulmonary, cardiac, and neurological LC [22, 26, 50, 51] and IL6
488 production induced by broad-spectrum mitogen PMA was found to be elevated in individuals
489 with LC [20]. These data together bolster the notion of targeting IL6 as a potential LC therapeutic
490 strategy.
491 Most striking from our study was the finding that while fully recovered individuals
492 exhibited coordinated humoral and cellular immune responses to SARS-CoV-2, this
493 coordination was lost in the LC group. This finding is consistent with observations that about half
494 of individuals with LC with no detectable SARS-CoV-2 antibodies have detectable SARS-CoV-
495 2-specific T cell responses [52]. That improper crosstalk between T and B cells may be involved in
496 the etiology of LC is also supported by our RNAseq data, which showed that a cluster of genes
497 including both immunoglobulin synthesis and T cell function were co-upregulated in those
498 without LC, but not in individuals with LC. The downregulation of immunoglobulin-related genes
499 in the context of LC has previously been reported and shown to be independent of spike
500 antibody levels [40], which is in line with our finding higher levels of spike antibodies in our
501 individuals with LC. How the humoral response becomes divorced from the cellular response is
502 unclear, and could potentially involve a mis-alignment between IL4 and IL5 production by Th2
503 cells which emerged from our Olink analysis. Potential upstream initiators leading to the mis-

504 coordination include a long-lived SARS-CoV-2 reservoir, reactivation of viral co-infections, or
505 autoimmune responses.
506 Finally, our datasets taken together point to not only a dysregulated but also a highly
507 pro-inflammatory signature in LC, consistent with prior data suggesting elevated and persistent
508 inflammation in LC [22, 23, 31, 50, 51]. Of particular interest was the elevation of the SGALS9 gene
509 product in LC. LGALS9 encodes for Galectin 9, which has previously been shown to be
510 upregulated during acute COVID-19 and may be a contributing factor in cytokine release and
511 subsequent disease severity [53, 54, 55]. The high inflammatory state observed in our individuals
512 with LC may be in part driven by immune dysregulation, which could initiate from improper
513 cross-talk between T and B cells as discussed above, or potentially faulty regulatory
514 mechanisms as supported by our observation that the individuals with LC with the highest
515 frequencies of exhausted SARS-CoV-2-specific CD8+ T cells were those that had the lowest
516 frequencies SARS-CoV-2-specific CD4+ Treg cells. Non-immune mechanisms may also be at
517 play, as supported by our findings that genes involved in olfactory sensing and heme synthesis
518 were also upregulated in those with LC. The findings of increased heme synthesis were
519 interesting in light of the fact that higher expression of genes involved in heme biosynthesis
520 (among T cells, B cells, and monocytes) are observed during acute COVID-19 [56, 57], and that
521 SARS-CoV-2 can bind hemoglobin and dysregulate heme metabolism [58, 59, 60]. It is also possible
522 that increased heme synthesis may reflect fibrin amyloid microclot formation that has been
523 observed in individuals with LC [10, 61], and is of interest in light of our finding increased platelet
524 numbers in the LC donors we analyzed by scRNAseq. These microclots appear to be resistant
525 to fibrinolizes and may trap potential circulating biomarkers of the coagulopathy [62, 63]. As a
526 result, heme synthesis may play a useful role in determining the extent of microclot formation.
527 Further studies of iron metabolism and red blood cell function, and their relationships to
528 coagulopathy in the setting of LC, are warranted.
529 Our study has several limitations. The analysis cohort included only 43 participants due to
530 our strict definitions of LC and complete recovery as detailed above. However, such rigor with
531 which the participants were characterized, and their consistency in meeting the case definition
532 longitudinally, mitigates the limitations of our small sample size, and we believe is a major strength
533 of our study. We also note that the parent cohort is a convenience sample and certainly not
534 representative of all individuals with a history of SARS-CoV-2 infection, although it did reflect the
535 characteristics of the pandemic in our geographic region. Some findings we report were driven by
536 small subsets of LC patients, which is consistent with the notion of LC being a very heterogeneous
537 disease, and requires validation in larger cohorts. A second limitation was our focus on blood
538 specimens, when the source of immune dysregulation, including SARS-CoV-2 persistence, likely
539 originates from tissues, and changes in subset frequencies in blood could reflect migration into
540 tissues. The infrastructure supporting LIINC has the ability for non-invasive tissue sampling via
541 gut biopsies and fine needle aspirates [64, 65], and future studies will take advantage of these
542 capabilities to better understand the tissue-based mechanisms underlying the immune
543 dysregulation that manifests in LC. Finally, we note that our study is for the most part descriptive,
544 but as for any such new and poorly-understood disease for which currently there is no good animal
545 model, such in-depth "omics"-based characterization of a well-annotated cohort is the critical first
546 step for better understanding the condition's etiology and mechanistic underpinnings.
547 Overall, we found using multiple analytical approaches in a carefully selected cohort of
548 individuals with consistent post-COVID symptom trajectories that LC is associated with
549 dysregulation between humoral and cellular immunity. While LC exhibits both clinical and
550 biological complexity, this work contributes to a growing understanding of the potential
551 pathophysiological contributors and suggests several mechanisms warranting further exploration
552 and/or disruption in future therapeutic trials.
553

ACKNOWLEDGEMENTS

This work was supported by the Van Auken Private Foundation, David Henke, and Pamela and Edward Taft; philanthropic funds donated to Gladstone Institutes by The Roddenberry Foundation and individual donors devoted to COVID-19 research; the Program for Breakthrough Biomedical Research, which is partly funded by the Sandler Foundation; and Awards #2164 and #2208 from Fast Grants, a part of Emergent Ventures at the Mercatus Center, George Mason University. We acknowledge the NIH DRC Center Grant P30 DK063720 and the S10 1S10OD018040-01 for use of the CyTOF instrument, and the NIH S10 RR028962 and the James B. Pendleton Charitable Trust for use of the Fortessa X-20. This study was also funded by the Ministerium für Wissenschaft, Forschung und Kunst, Baden Württemberg, Germany (KNKC.031) and the Deutsche Forschungsgemeinschaft (DFG, German Research Foundation)—Projektnummer 316249678—SFB 1279. The parent cohort (LIINC) is supported by NIH/NIAID 3R01AI141003-03S1 and NIH/NIAID R01AI158013. We thank Stanley Tamaki, Vinh Nguyen, Pricsilla Sanchez and Claudia Bispo for CyTOF assistance at the Parnassus Flow Core, Jane Srivastava and Vaishanavi Saware for technical assistance in FACS, Merve Karacan and Nico Preising for technical assistance in peptide synthesis, Eliver Ghosn for guidance on annotation of cell clusters identified by scRNAseq, John Carroll for assistance on graphics, Françoise Chanut for editorial assistance, and Robin Givens for administrative assistance.

We are grateful to the study participants and their medical providers. We acknowledge current and former LIINC clinical study team members Tamara Abualhsan, Andrea Alvarez, Mireya Arreguin, Melissa Buitrago, Monika Deswal, Nicole DelCastillo, Emily Fehrman, Halle Grebe, Heather Hartig, Yanel Hernandez, Marian Kerbleski, Raushun Kirtikar, James Lombardo, Michael Luna, Lynn Ngo, Enrique Martinez Ortiz, Antonio Rodriguez, Justin Romero, Dylan Ryder, Ruth Diaz Sanchez, Matthew So, Celina Song, Viva Tai, Alex Tang, Cassandra Thanh, Fatima Ticas, Leonel Torres, Brandon Tran, Deepshika Varma, and Meghann Williams; and LIINC laboratory team members Amanda Buck, Joanna Donatelli, Jill Hakim, Nikita Iyer, Owen Janson, Brian LaFranchi, Christopher Nixon, Isaac Thomas, and Keirstinne Turcios. We thank Jessica Chen, Aidan Donovan, and Carrie Forman for assistance with data entry and review. We thank the UCSF AIDS Specimen Bank for processing specimens and maintaining the LIINC biospecimen repository. We are grateful to Elnaz Eilkhani and Monika Deswal for regulatory support. We are also grateful for the contributions of additional current and former LIINC leadership team members: Matthew Durstenfeld, Priscilla Hsue, Bryan Greenhouse, Isabelle Rodriguez-Barraquer, and Rachel Rutishauser.

AUTHOR CONTRIBUTIONS

K.Y. designed the experiments, performed CyTOF, FACS, and scRNAseq experiments, conducted analyses, prepared figures and tables, and wrote the manuscript; M.J.P. designed the LIINC cohort, oversaw LIINC cohort procedures, interpreted data, and wrote the manuscript; X.L. developed pipelines for data analyses and performed scRNAseq; R.T. performed clustering and scRNAseq analyses; M.S. performed RNAseq and Olink analyses; J.N. prepared peptides and helped with experiments; A.A. and K.Y. prepared and analyzed CyTOF specimens, T.M. designed protocols for CyTOF analyses; R.H., K.A. and B.H. managed the LIINC cohort, recruited participants, collected clinical data, and collected biospecimens; U.A., M.L., D.V., K.A., T.D., and S.E.M. recruited LIINC participants, collected clinical data, and collected biospecimens; T.D. and S.E.M. processed specimens; L.S. and J.M. synthesized peptides; R.I. entered, cleaned, and performed quality control on LIINC data; S.L. and S.A.G. managed LIINC data and selected biospecimens; K.L.L. performed antibody assays; S.A.L. designed the CHIRP cohort and oversaw CHIRP cohort procedures; J.D.K. and J.N.M designed the LIINC cohort and interpreted LIINC clinical data; S.G.D. designed the LIINC cohort, oversaw cohort procedures, and interpreted LIINC clinical data; T.J.H. designed the LIINC cohort, oversaw cohort procedures, performed the RNAseq and Olink studies, interpreted data, prepared figures, and wrote the manuscript; N.R.R.

conceived the study, performed supervision, conducted data analyses, prepared figures and tables, and wrote the manuscript. All authors have read and approved this manuscript.

CONFLICTS OF INTERESTS

MJP reports consulting fees from Gilead Sciences and AstraZeneca, outside the submitted work. SGD reports grants and/or personal fees from Gilead Sciences, Merck & Co., Viiv, AbbVie, Eli Lilly, ByroLogyx, and Enochian Biosciences, outside the submitted work. TJH receives grant support from Merck and consults for Roche. All other authors report no potential conflicts.

Methods

Study participants

Participants were volunteers in the University of California, San Francisco (UCSF)-based Long-term Impact of Infection with Novel Coronavirus (LIINC) cohort (www.liincstudy.org; NCT04362150). Details of cohort recruitment, enrollment, and measurement procedures have been described in detail previously [37]. Briefly, LIINC is a prospective observational study enrolling individuals with prior nucleic acid-confirmed SARS-CoV-2 infection in the San Francisco Bay Area, regardless of the presence or absence of post-acute symptoms. At each study visit, participants underwent an interviewer-administered assessment of 32 physical symptoms that were newly developed or had worsened since COVID-19 diagnosis, as well as assessment of mental health and quality of life. Pre-existing and unchanged symptoms were not considered to be attributable to COVID-19. In addition, detailed data regarding medical history, COVID-19 history, SARS-CoV-2 vaccination, and SARS-CoV-2 reinfection were collected. The majority of participants in LIINC did not require hospitalization for COVID-19 and were treated with symptomatic management or observation during the acute phase of infection [37]. Consistent with broader epidemiologic trends [66], individuals with LC in LIINC are more likely to be female and have higher body mass index (BMI). Other pre-existing medical comorbidities are relatively uncommon in the LIINC, although we generally observe a higher rate of hypertension among those with LC compared to those who fully recovered [23]. Two participants enrolled in LIINC had biospecimens collected previously via the UCSF COVID-19 Host Immune Response Pathogenesis (CHIRP) study, which utilizes identical procedures for ascertainment of clinical history as the LIINC study [35].

Because of challenges in the measurement of LC as outlined in prior work from the LIINC cohort, including within-participant symptom variability as well as the fact that some individuals with LC demonstrate symptomatic improvement and resolution of symptoms over time [37], we selected for this analysis participants who consistently met a case definition for LC based on the presence or absence of at least one symptom attributable to COVID-19 for the 8-month period following SARS-CoV-2 infection (Fig. S1A). The LC group (n=27) included individuals who consistently reported at least 1 COVID-19 attributed symptom during the entire study period, while the non-LC group (n=16) included individuals who consistently reported no COVID-19 attributed symptoms during the entire study period. Because of the potential effects of SARS-CoV-2 vaccination on clinical symptoms of LC as well as the immunologic measurements conducted in this study, we restricted the participants to those who provided a post-COVID blood sample prior to having ever received a SARS-CoV-2 vaccination. Blood samples were collected between September 16, 2020, and April 6, 2021.

Biospecimen Collection

At each visit, whole blood was collected in EDTA tubes followed by density gradient separation and isolation of PBMCs and plasma, as described previously [31]. Serum was obtained concomitantly from serum-separator tubes. Serum and plasma were stored at -80°C and PBMCs were cryopreserved and stored in liquid nitrogen.

Antibody Assays

Antibody responses against SARS-CoV-2 spike RBD were measured on sera using the Pylon COVID-19 total antibody assay (ET Health). The assay's lower limit of detection was 10 relative fluorescence units (RFUs).

SARS-CoV-2 peptide pool

Peptides used for T cell stimulation comprised a mix of overlapping 15-mers spanning the entire SARS-CoV-2 spike protein (PM-WCPV-S-1, purchased from JPT), and peptides corresponding

665 to CD8+ T cell epitopes identified by T-scan [67] which were synthesized in-house (Table S6). The
666 final concentration of 15-mer peptides was 300 nM and the final concentration of T-scan peptides
667 was 450 nM.
668
669 ***CyTOF antibody conjugation***
670 CyTOF antibody conjugation was performed using the Maxpar® X8 Antibody Labeling Kit
671 (Standard BioTools) according to manufacturer's instructions with some modifications. Briefly,
672 0.1 mg Maxpar Polymer Reagent was first dissolved in 95 µl L-buffer, and then 5 µl lanthanide
673 solution was added into the polymer. Following a 60-min incubation at room temperature (RT),
674 the polymer mixture was transferred into a 3-kD Amicon™ Ultra tube (Fisher) and centrifuged at
675 12,000 g for 25 min at RT. The retentate was then washed with 400 µl C-buffer, centrifuged
676 again, and flowthrough was discarded. Next, 100 µg antibody was mixed with 200 µl R-buffer
677 and transferred to a 50-kD Amicon™ Ultra tube (Fisher), and then centrifuged at 12,000 g for 10
678 min at RT. Next, 100 µl TCEP (Pierce) diluted in R-buffer (4mM final concentration) was added
679 to the buffer-exchanged antibody retentate on the column, followed by vortexing and then a 30-
680 min incubation at 37°C. We then added 300 µl C-buffer to the antibody mix, centrifuged the
681 mixture at 12,000 g for 10 min at RT, washed with 400 µl C-buffer, then centrifuged again. Next,
682 200 µl C-buffer was added to resuspend the polymer (in the 3-kD Amicon™ Ultra tube), which
683 was then transferred to the antibody column and placed in a new collection tube. Following a
684 60-min incubation at 37°C, 300 µl W-buffer was added into the antibody conjugation mix. The
685 column was then centrifuged at 12,000 g for 10 min at RT and washed three times with 400 µl
686 W-buffer through sequential centrifugation and discarding of flowthrough. Finally, 50 µl W-buffer
687 was added to the column, which was centrifuged for 2 min at 1,000 g. The flowthrough in the
688 bottom collection tube was then collected to recover the conjugated CyTOF antibody. The last
689 collection step was repeated a total of two times and eluted material combined.
690
691 ***Sample preparation for CyTOF***
692 Sample preparation was performed similarly to methods previously described [32, 33, 34, 35] with some
693 modifications. Briefly, PBMCs were isolated from fresh blood draws from the LIINC participants
694 and cryopreserved. Upon revival, cells were rested overnight to allow for antigen recovery [68], and
695 then divided equally into two aliquots. To the first aliquot, we added 3 µg/ml brefeldin A (BFA, to
696 enable intracellular cytokine detection), the co-stimulation agonists anti-CD28 (2 µg/ml, BD
697 Biosciences) and anti-CD49d (1 µg/ml, BD Biosciences), and the SARS-CoV-2 peptide pool
698 prepared as described above. To the second aliquot, we added only 1% DMSO (Sigma) and 3
699 µg/ml BFA. Cells from both treatments were incubated at 37°C for 6 h. Thereafter, cells were
700 treated with cisplatin (Sigma) as a live/dead distinguisher and then fixed in paraformaldehyde
701 (PFA, Electron Microscopy Science) using methods similar to those recently implemented [32, 33, 34,
702 35]. Briefly, 6 million cells were resuspended in 4 ml of PBS (Rockland) containing 2 mM EDTA
703 (Corning) and 25 µM cisplatin (Sigma), and incubated for 60 seconds. Cells were then washed
704 twice in 1 ml CyFACS (containing 0.1% Bovine Serum Albumin (Sigma) and 0.1% Sodium Azide
705 (Sigma) in PBS) and fixed for 10 mins at room temperature in 1.2 ml 2% PFA diluted in CyFACS.
706 Cells were then washed twice with 1 ml CyFACS, resuspended in 100 µl 10% DMSO (Sigma)
707 diluted in CyFACS, and frozen at -80℃ until CyTOF staining. PBMCs from a healthy donor were
708 also subjected to the same cisplatin/fixation protocol and then aliquoted, and served as bridge
709 samples for batch correction.
710
711 CyTOF staining was performed similar to methods recently described, where we made
712 precautions to avoid EDTA during all CyTOF staining steps as EDTA can interfere with chemokine
713 receptor staining [32, 33, 34, 35]. Cisplatin-treated and PFA-fixed specimens were barcoded using Cell-
714 ID™ 20-Plex Pd Barcoding Kit (Standard BioTools) according to manufacturer's instructions. After
715 barcoding, cells from up to 20 different samples were then combined into a single sample, at a

716 concentration of 6 million cells per sample in 100 µl. The cells were then blocked at 4℃ for 15
717 mins in 200 µl CyFACS buffer containing 3 µl rat serum (Invitrogen), 3 µl mouse serum (Invitrogen),
718 and 0.6 µl human serum (Sigma). After two washes with CyFACS, cells were subjected to surface
719 antibody staining by resuspending the cells in 100 µl of freshly-prepared cell surface antibody mix
720 (Table S2). Staining was allowed to proceed for 45 mins at 4℃. After 3 washes with CyFACS,
721 cells were fixed overnight in 100 µl 2% PFA diluted in PBS. The next day, cells were washed with
722 CyFACS and permeabilized by resuspension in 200 µl Foxp3 fix/perm buffer (eBioscience), and
723 incubated at 4℃ for 30 mins. The cells were pelleted and then blocked at 4℃ for 15 mins by
724 addition of a pre-mixed solution of 15 µl mouse serum, 15 µl rat serum, and 70 µl permeabilization
725 Buffer (eBioscience). The cells were then washed in 800 µl permeabilization buffer (eBioscience),
726 and incubated at 4℃ for 45 mins in 100 µl freshly-prepared intracellular staining antibody mix
727 (Table S2). After another two washes with CyFACS, cells were stained with 250 nM Intercalator-
728 IR (Standard BioTools) at room temperature for 20 mins. Finally, after two additional washes with
729 CyFACS, the cells were then fixed with 1 ml 2% PFA diluted in CyFACS.
730
731 ***CyTOF data acquisition***
732 The PFA-fixed samples were washed twice with CAS buffer (Standard BioTools) and then spiked
733 with 10% (v/v) EQ™ Four Element Calibration Beads (Standard BioTools) diluted in CAS buffer,
734 before loading onto a Helios CyTOF instrument (UCSF Parnassus Flow Core). A running speed
735 of 200 to 400 events per second was maintained during sample collection, and the loading voltage
736 was controlled between 4 and 5 to minimize clogging. Data were normalized to EQ beads by
737 CyTOF software provided by Standard BioTools to batch-correct for instrument sensitivity during
738 sample collection. Data matrices were exported as flow cytometry standard (fcs) files for data
739 analyses as described below.
740
741 ***T cell CyTOF data analyses***
742 **Data preprocessing.** EQ bead-normalized CyTOF datasets were concatenated, de-barcoded,
743 and normalized using CyTOF software provided by Standard BioTools (version 6.7) according to
744 manufacturer's instructions. Following arcsinh transformation of the data as described [69], cells
745 were then analyzed by FlowJo (version 10.8.1, BD Biosciences). Intact (Ir191+Ir193+), live
746 (Pt195-), singlet events were identified as described in Fig. S2A, B. Those events were then gated
747 on T cells (CD3+) followed by sub-gating on CD4+ T cells and CD8+ T cells (Fig. S2A, B).
748
749 **CyTOF antibody validation.** Our CyTOF panel (Table S2) was designed to incorporate markers
750 commonly used to define T cell subsets (e.g., CD4, CD8α, CD45RA, CD45RO, CCR7, CD27,
751 CD95, PD1, CXCR5, CD25, CD127, Foxp3), activation states (e.g., CD38, ICOS, CD25, Ox40,
752 Ki67, CD69, HLADR), exhaustion states (e.g., PD1, CTLA4, TIGIT), homing properties (e.g.,
753 CCR6, CCR5, CXCR4, CD62L, CD29, CCR7, CXCR5), and effector function (e.g., IFNγ, TNFα,
754 IL2, IL4, IL6, IL17, MIP1β, Granzyme B, perforin). Some of these markers were previously
755 associated with immune responses to COVID-19 [34]. CyTOF antibodies were validated using
756 methods previously described [32, 33, 34, 35, 65, 69], by demonstrating expected expression patterns
757 among and between immune subsets. Antigen expression patterns detected using the CyTOF
758 antibodies used in this study were similar to those previously observed [32, 33, 34, 35, 65, 69]. Fig. S18
759 illustrates some examples of CyTOF antibody validation implemented for this study. CyTOF
760 analysis of human lymphoid aggregate cultures generated from fresh tonsils were performed as
761 described [69]. The observed expression patterns among tonsillar T and B cells (Fig. S18A) were
762 similar to those previously observed and validated [69]. To validate detection of cytokines and other
763 effector molecules, we stimulated PBMCs with 16 nM PMA (Sigma) and 1 µM ionomycin (Sigma),
764 or 1 µg/ml LPS (eBioscience), for 4 hours in the presence of 3 µg/ml brefeldin A solution
765 (eBioscience), and then cisplatin-treated and PFA-fixed the cells as described above. Cells from

766 the two stimulation conditions were then combined. We observed the expected induction of
767 cytokines or cytolytic markers among these cells (Fig. S18B) [32, 33, 34, 35]. We observed preferential
768 expression of Treg lineage marker Foxp3 among our gated population of Treg cells (Fig. S18C),
769 and preferential expression of CD30 and Ki67 in memory as compared to naïve CD4+ T cells (Fig.
770 S18D) as expected, thereby validating these lowly-expressed antigens. An example of peripheral
771 Tfh gate establishment is depicted in Fig. S18E, where we gated on memory CD4+ T cells
772 expressing high levels of CXCR5 and PD1.
773
774 **Identification of SARS-CoV-2-specific T cells.** For identification and definition of SARS-CoV-
775 2-specific T cells, we compared unstimulated specimens to their peptide-stimulated counterparts.
776 Effector cytokines (IFNγ, TNFα, IL2, IL4, IL6, IL17, MIP1β), cytolytic effectors (Granzyme B and
777 perforin) and LAMP1 were assessed for the ability to identify antigen-specific T cells at the single-
778 cell level. Of note, in our system, as the antibody against LAMP1 was added during intracellular
779 staining and not at the time of peptide stimulation, it was not used as a degranulation marker, but
780 rather only to quantitate intracellular LAMP1 expression. The following criteria were established
781 to identify effector molecules appropriate for identifying SARS-CoV-2-specific T cells: 1) counts
782 of positive cells in unstimulated sample (not receiving peptide) was less than 5 events, or the
783 frequency of positive cells was lower than 0.1%; 2) counts of positive cells in the peptide-
784 stimulated sample was not less than 5, or the frequency was higher than 0.1%; 3) differences in
785 frequencies of positive cells between unstimulated and peptide-stimulated samples cells was not
786 less than 0.01%, 4) the fold-change in frequencies of positive cells between unstimulated and
787 peptide-stimulated samples cells was greater than 10; and 5) the aforementioned 4 criteria could
788 identify SARS-CoV-2-specific T cells among >50% of participants. Effectors which fulfilled all five
789 criteria for CD4+ T cells were IFNγ, TNFα, and IL2, and those which fulfilled all five criteria for
790 CD8+ T cells were IFNγ, TNFα, and MIP1β. For a sub-analysis to identify responding cells that
791 may only exist in a small subset of individuals, we removed criteria #5 and reduced the positive
792 cell counts to number 3 within criteria #1 and #2. This approach allowed us to determine that
793 SARS-CoV-2-specific CD4+ T cells producing IL6 were exclusively detected from LC (Fig. S3D).
794 Of note, activation induced markers (AIM) such as Ox40, CD69, and CD38 were not used to
795 identify SARS-CoV-2-specific T cells because they cannot specifically distinguish these cells from
796 bystander T cells after a 6-hour stimulation [34]. SARS-CoV-2-specific T cells were detected at a
797 median of 163 cells (134 for CD4+ T cells, 29 for CD8+ T cells), and a mean of 221.7 cells (185.2
798 for CD4+ T cells, 36.4 for CD8+ T cells), per participant. SARS-CoV-2-specific T cells, once
799 identified, were analyzed by Boolean gating [70] and exported for further analyses.
800
801 **SPICE.** SPICE analyses were performed similar to previously described methods [71]. Briefly, CD4+
802 and CD8+ T cells were subjected to manual gating based on expression of cytokines used to
803 define SARS-CoV-2-specific T cells (IFNγ, TNFα, IL2, and MIP1β, see above) using operations
804 of Boolean logic. The dataset matrix generated from Boolean gating was then inputted into SPICE
805 software (version 6.1) for polyfunctional analysis. The parameters for running the dataset were:
806 iterations for permutation test = 10,000, and highlight values = 0.05. The parameters for the query
807 structure were set as follows: values = frequency of single cytokine positive cells in total
808 CD4+/CD8+ T cells (generated directly from FlowJo); category = IFNγ, TNFα, IL2, and MIP1β;
809 overlay = patient type (LC vs. Non-LC); group = all other variables in the data matrix (including
810 sex, PID, cell type, hospitalization status, and batch). All other parameters for SPICE analyses
811 were kept as default.
812
813 **T cell subsetting.** Manual gating was performed using R (version 4.1.3). Briefly, arcsinh-
814 transformed data corresponding to total or SARS-CoV-2-specific T cells were plotted as 2D plots
815 using the CytoExploreR package. Statistical data were then exported for further analyses.
816 Visualization of datasets by tSNE were performed using R (version 4.1.3), using methods similar

817 to those previously described [32, 33, 34, 35]. Briefly, CytoExploreR and tidyr packages were used to
818 load the data. tSNE was performed using Rtsne and RColorBrewer packages on arcsinh-
819 transformed markers. Total CD4+/CD8+ T cells were downsampled to n = 8000 (maximal cell
820 number for individual samples) before tSNE analysis. The parameters for tSNE were set as
821 follows: iteration = 1000, perplexity = 30, and theta= 0.5.
822
823 **T cell clustering analysis.** FCS files corresponding to total and SARS-CoV-2 specific CD4+ and
824 CD8+ T cells were imported in R for data transformation. Packages of flowcore, expss, class, and
825 openxlsx were loaded in R for training FCS files. Arcsinh-transformed data were then exported
826 as csv files for clustering analyses. Biological (LC status, biological sex, hospitalization status)
827 and technical (batch/run of processing) variables were visualized using the DimPlot function in
828 the Seurat package [72]. As batch effects associated with the processing run were evident, batch
829 correction was performed across the 6 batches using the harmony [73] batch correction function
830 RunHarmony, applied to the marker levels in cells. The optimal clustering resolution parameters
831 were determined using Random Forests [74] and a silhouette score-based assessment of clustering
832 validity and subject-wise cross-validation. This procedure is described in greater detail in George
833 et al. [64]. A generalized linear mixed model (GLMM) (implemented in the lme4 [75] package in R with
834 family argument set to the binomial probability distribution) was used to estimate the association
835 between cluster membership and LC status and the biological sex of the participant, with the
836 participant modeled as a random effect. For each given participant, cluster membership of cells
837 is encoded as a pair of numbers representing the number of cells in the cluster and the number
838 of cells not in the cluster. Clusters having fewer than 3 cells were discarded. The sex-specific log
839 odds ratio of cluster membership association with LC status was estimated using the emmeans
840 [76] R package using the GLMM model fit. The estimated log odds ratio represents the change (due
841 to LC status) in the average over all participants of a given sex in the log odds of cluster
842 membership. The two-sided p-values corresponding to the null hypothesis of an odds ratio value
843 of 1 was computed based on a Z-statistic in the GLMM model fit. These p-values were adjusted
844 for multiple testing using the Benjamini-Hochberg method.
845
846 ***FACS***
847 Validation experiments using flow cytometry (FACS) was performed on total PBMCs from n=40
848 individuals in our cohort (25 LC, 15 non-LC). Sample preparation and cell revival were performed
849 as described above for CyTOF preparation, and analyzed at baseline, or following SARS-CoV-2
850 peptide stimulation. For staining, cells were first treated with Zombie UV™ or Zombie NIR™
851 (BioLegend) as viability indicators, and then blocked with Human TruStain FcX™ (BioLegend).
852 FACS antibodies that were used in this study are shown in Table S7. For intracellular staining,
853 cells were fixed with 2% PFA and incubated with Foxp3 fix/perm buffer (eBioscience) per
854 manufacturer's instructions, following completion of surface antibody staining. The BD Horizon™
855 Brilliant stain buffer (BD Biosciences) was used according to manufacturer's instructions when
856 staining with antibodies conjugated to brilliant dyes. All cells were fixed in 2% PFA prior to analysis
857 on a Fortessa X-20 (BD Biosciences). UltraComp eBeads™ Compensation Beads (Invitrogen)
858 served as a single fluorescence dye control, and ArC™ Amine Reactive Compensation Beads
859 (Invitrogen) served as a loading control for live/dead cell staining. FCS files were exported into
860 FlowJo (BD, version 10.9.0) for further analyses. FACS data were arcsinh-scaled prior to analyses.
861
862 ***RNAseq***
863 RNAseq was performed on total PBMCs from n=36 individuals in our cohort using the AllPrep kit
864 as per manufacturer's instructions (Qiagen). RNA libraries, next generation Illumina sequencing,
865 quality control analysis, trimming, and alignment to the human genome (hg19) were performed
866 by Genewiz (Azenta Inc.). Briefly, following oligo dT enrichment, fragmentation and random
867 priming, cDNA syntheses was completed. End repair, 5' phosphorylation and dA-tailing were

868 performed, followed by adaptor ligation, PCR enrichment, and sequencing on an Illumina HiSeq
869 platform using PE150 (paired-end sequencing, 150 bp for reads 1 and reads 2). Raw reads (480
870 Gb in total) were trimmed using Trimmomatic (version 0.36) to remove adapter sequences and
871 poor-quality reads. Trimmed reads were then mapped to Homo sapiens GRCh37 using star
872 aligner (version 2.5.2b) [77]. Log2 fold-changes were calculated between those with or without any
873 LC symptoms. Two-sided P values corresponding to a null hypothesis of fold-change of 1 were
874 calculated using DESeq2's [78] Wald test, and were adjusted controlling for multiple testing using
875 false discovery rates. Genes with an adjusted p-value < 0.05 and absolute log2 fold-change > 1
876 were considered as significantly differentially expressed genes (DEGs). Clustered heatmaps of
877 DEG were constructed with groups of genes (rows) defined using the k-means algorithm to
878 cluster genes into k clusters based on their similarity. K = 4 was determined using the
879 HOPACH (Hierarchical Ordered Partitioning and Collapsing Hybrid) algorithm [79],
880 which recursively partitions a hierarchical tree while ordering and collapsing clusters at each
881 level to identify the level of the tree with maximally homogeneous clusters.
882
883 ***scRNAseq***
884 scRNAseq library preparation was performed on total PBMCs from n=12 individuals (4 non-LCs
885 and 8 LCs) in our cohort using the Chromium Next GEM Single Cell 5' Reagent Kits v2 (10x
886 Genomics) according to manufacturer's instruction. This was then followed by sequencing on
887 the Illumina NovaSeq 6000 S4 300 platform (UCSF Center for Advanced Technology). All 12
888 samples were sequenced at a mean of >50K reads per cell (minimum 51K, maximum 120K,
889 median 83K). A total of 1.3Tb sequencing data was collected. A median of 7888 cells was
890 analyzed per donor (minimum 4189, maximum 9511). Demultiplexed fastq files were aligned to
891 the human reference genome (GRCh38) using the 10x Genomics Cell Ranger v7.1.0 count
892 pipeline [80], as described in the Cell Ranger documentation. The include-introns flag for the
893 count pipeline was set to true to count reads mapping to intronic regions.
894 The filtered count matrices generated by the Cell Ranger count pipeline were processed
895 using the R package for using Seurat [72]. Each sample was pre-processed as a Seurat object,
896 and the top 1% of cells per sample with highest numbers of unique genes, cells with <=200
897 unique genes, and cells >=10% mitochondrial genes were filtered out for each sample. The 12
898 samples were then merged into a single Seurat object, and normalization and variance
899 stabilization was performed using sctransform86 with the "glmGamPoi" method [81] for initial
900 parameter estimation.
901 Graph-based clustering was performed using the Seurat [72] functions FindNeighbors and
902 FindClusters. First, the cells were embedded in a k-nearest neighbor (KNN) graph (with k=20)
903 based on the Euclidean distance in the PCA space. The edge weights between two cells were
904 further modified using Jaccard similarity. Next, clustering was performed using the Louvain
905 algorithm [82] implementation in the FindClusters Seurat function. Clustering with 15 Principal
906 Components (PCs) (determined based on location of elbow in the plot of variance explained by
907 each of the top 25 PCs) and 0.1 resolution (determined using the resolution optimization method
908 described above for CyTOF data clustering analyses) resulted in 11 distinct biologically relevant
909 clusters (Clusters 0-11), which were used for further analyses.
910 Data visualization using Seurat in UMAP space for the 12 samples revealed no apparent
911 batch effects due to age, sex (all were female), race, or hospitalization status of the subjects. The
912 marker genes for each cluster were identified using the FindAllMarkers Seurat function. This
913 algorithm uses the Wilcoxon Rank Sum test to iteratively identify DEGs in a cluster against all the
914 other clusters. Marker genes were filtered to keep only positively expressed genes, detected in at
915 least 25% of the cells, and with at least 0.5 log2 fold change. Cluster annotation was performed
916 according to subset definitions previously established [83, 84, 85]. Classification markers included
917 CD19, MS4A1, and CD79A for B cells; CD3D, CD3E, CD5, and IL7R for CD4+ T cells; CD3D,
918 CD3E, CD8A, CD8B, and GZMK (CTL subset) for CD8+ T cells; CD14, CD68, CYBB, S100A8,

S100A9, S100A12, and LYZ for monocytes; CSF2RA, LYZ, CXCL8, and CD63 for granulocytes; and PF4, CAVIN2, PPBP, GNG11, and CLU for platelets.

The Counts-Per-Million (CPM) (pseudo-bulked) reads for ALAS2 and OR7D2 were assessed in each of the subjects using edgeR [86], and associations with group status were using the two sample Welch t-test, followed by multiple correction testing using the Holm [87] procedure. For establishing associations between clusters and group status, GLMM implemented in the lme4 R package was used separately for each cluster of cells. The model was performed with the family argument set to the binomial probability distribution, and with the 'nAGQ' parameter set to 10 corresponding to the number of points per axis for evaluating the adaptive Gauss-Hermite approximation for the log-likelihood estimation. Cluster membership of cells by sample was modeled as a response variable by a 2-dimensional vector representing the numbers of cells from a given sample belonging or not to the cluster under consideration. The corresponding sample from which the cell was derived was the random effect variable, and the group (non-LC, LC, ORD72^{high} LC, or ALAS2^{high} LC) was considered the fixed variable. The log odds ratio for all pairwise comparisons were estimated using the model fits provided to the emmeans function in the emmeans R package [76]. The resulting p-values for the estimated log odds ratio and clusters were adjusted for multiple testing using the Benjamini-Hochberg method [88]. For associations of gene expression with group status within each cluster, the raw gene counts per cell were loaded as a SingleCellExperiment object. Cells from clusters 9 and 10 were not included in this analysis as the median number of cells across samples was less than 20 for each of these clusters. The aggregateData function in the muscat bioconductor package [89] was used to pseudo-bulk the gene read counts across cells for each cluster group. Genes with raw counts less than 10 in more than 8 samples were removed from the analyses. The pbDS function implementing the statistical methods in the edgeR package [86] was used to assess associations of gene expression with group identity in each of the clusters.

Olink

We performed the Olink EXPLORE 384 inflammation Protein Extension Assay (PEA) from plasma from n=40 individuals in our cohort to characterize 384 unique plasma proteins associated with inflammation and immune signaling. PEA involves dual-recognition of two matched antibodies labelled with unique DNA oligonucleotides that simultaneously bind to specific target proteins. The simultaneous antibody binding leads to hybridization of unique DNA oligonucleotides that serve as templates for polymerase-dependent extension (DNA barcoding) followed by PCR amplification and NovaSeq (Illumina) DNA sequencing as published [90, 91, 92, 93, 94]. A similar analysis pipeline was applied to the protein biomarkers as described for the gene expression data as above.

Data visualization for RNAseq and Olink

To generate heatmaps, the R package HOPACH [79] was used to find the best cluster number. Gene expression values were log-transformed and centered using the average expression value for each gene. Genes were clustered by running the Kmeans algorithm using the best cluster number K found, and the results were plotted using the pheatmap package [95]. For gene network analyses, the STRING interaction database was used to reconstruct gene networks using stringApp [96] for Cytoscape [97]. For the network, the top 50 genes or 25 proteins with the lowest p-values were selected from the RNAseq data and Olink data, respectively. Then genes were subjected to stringApp with an interaction score cutoff = 0.5, and the number of maximum additional indirect interactors cutoff = 10. The analysis integrated STRING data with our gene inputs, resulting in a network of 24 nodes and 100 edges in for the RNAseq data, and a network of 26 nodes and 165 edges for the Olink data. In each network, a node corresponds to a gene, an edge represents the functional relevance between a pair of genes, with the thickness of each edge reflecting the confidence level. Node color indicates the degree of log2 fold-change and the difference between protein expression values for the RNAseq and Olink data, respectively.

970
971 ***Data availability***
972 The raw CyTOF datasets for this study corresponding to total and SARS-CoV-2-specific CD4+
973 and CD8+ T cells are publicly accessible through the following link:
974 https://datadryad.org/stash/share/TE_QuY0JX23V2n2CIMO2PgsR6aflp6GGusdQ5nXVGnk.
975 The raw bulk RNAseq and scRNAseq data from this study are deposited in the GEO (Gene
976 Expression Omnibus) database: GSE224615 (for bulk RNAseq) and GSE235050 (for scRNAseq).
977 All other raw datasets from this study are available from the corresponding authors upon request.
978
979 ***Statistical tests***
980 Unless otherwise indicated, permutation tests, two-tailed unpaired student's t-tests, and Welch's
981 t test were used for statistical analyses. *$p < 0.05$, **$p < 0.01$, ***$p < 0.001$, ****$p<0.0001$, and n.s.
982 non-significant. Error bars corresponded to standard deviation (SD). Graphs were plotted by
983 GraphPad Prism (version 9.4.1). All measurements were taken from distinct samples, no samples
984 were measured repeatedly to generate data. Where appropriate, p-values were corrected for
985 multiple testing (across 3 pairwise comparisons) using the Holm procedure [87].
986
987 ***Informed consent***
988 All participants provided written informed consent and study protocols were approved by the
989 UCSF Institutional Review Board.

REFERENCES

1. Nalbandian, A. *et al.* Post-acute COVID-19 syndrome. *Nat. Med.* (2021).

2. Peluso, M.J. & Deeks, S.G. Early clues regarding the pathogenesis of long-COVID. *Trends Immunol.* **43**, 268-270 (2022).

3. Davis, H.E., McCorkell, L., Vogel, J.M. & Topol, E.J. Long COVID: major findings, mechanisms and recommendations. *Nature Reviews Microbiology*, 1-14 (2023).

4. Azzolini, E. *et al.* Association Between BNT162b2 Vaccination and Long COVID After Infections Not Requiring Hospitalization in Health Care Workers. *JAMA* (2022).

5. Ayoubkhani, D. *et al.* Trajectory of long covid symptoms after covid-19 vaccination: community based cohort study. *BMJ* **377**, e069676 (2022).

6. Al-Aly, Z., Bowe, B. & Xie, Y. Long COVID after breakthrough SARS-CoV-2 infection. *Nat. Med.*, 1-7 (2022).

7. Xie, Y., Choi, T. & Al-Aly, Z. Nirmatrelvir and the Risk of Post-Acute Sequelae of COVID-19.

8. Wynberg, E. *et al.* The effect of SARS-CoV-2 vaccination on post-acute sequelae of COVID-19 (PASC): A prospective cohort study. *Vaccine* **40**, 4424-4431 (2022).

9. Ambrosino, P. *et al.* Clinical assessment of endothelial function in convalescent COVID-19 patients: a meta-analysis with meta-regressions. *Ann. Med.* **54**, 3234-3249 (2022).

10. Pretorius, E. *et al.* Prevalence of symptoms, comorbidities, fibrin amyloid microclots and platelet pathology in individuals with Long COVID/Post-Acute Sequelae of COVID-19 (PASC). *Cardiovasc. Diabetol.* **21**, 148 (2022).

11. Seeßle, J. *et al.* Persistent symptoms in adult patients one year after COVID-19: a prospective cohort study. *Clin. Infect. Dis.* (2021).

12. Su, Y. *et al.* Multiple Early Factors Anticipate Post-Acute COVID-19 Sequelae. *Cell* **0** (2022).

13. Son, K. *et al.* Circulating anti-nuclear autoantibodies in COVID-19 survivors predict long-COVID symptoms. *Eur. Respir. J.* (2022).

14. Gold, J.E., Okyay, R.A., Licht, W.E. & Hurley, D.J. Investigation of long COVID prevalence and its relationship to Epstein-Barr virus reactivation. *Pathogens* **10**, 763 (2021).

15. Peluso, M.J. *et al.* Impact of pre-existing chronic viral infection and reactivation on the development of long COVID. *The Journal of Clinical Investigation* (2022).

1034 16. Stein, S.R. *et al.* SARS-CoV-2 infection and persistence in the human body and brain at
1035 autopsy. *Nature*, 1-6 (2022).
1036
1037 17. Peluso, M.J. *et al.* SARS-CoV-2 and Mitochondrial Proteins in Neural-Derived Exosomes of
1038 COVID-19. *Ann. Neurol.* (2022).
1039
1040 18. Swank, Z. *et al.* Persistent circulating SARS-CoV-2 spike is associated with post-acute
1041 COVID-19 sequelae. *Clin. Infect. Dis.* (2022).
1042
1043 19. Natarajan, A. *et al.* Gastrointestinal symptoms and fecal shedding of SARS-CoV-2 RNA
1044 suggest prolonged gastrointestinal infection. *Med (N Y)* (2022).
1045
1046 20. Klein, J. *et al.* Distinguishing features of Long COVID identified through immune profiling.
1047 *medRxiv* (2022).
1048
1049 21. Phetsouphanh, C. *et al.* Immunological dysfunction persists for 8 months following initial
1050 mild-to-moderate SARS-CoV-2 infection. *Nat. Immunol.*, 1-7 (2022).
1051
1052 22. Peluso, M.J. *et al.* Markers of Immune Activation and Inflammation in Individuals With
1053 Postacute Sequelae of Severe Acute Respiratory Syndrome Coronavirus 2 Infection. *J.*
1054 *Infect. Dis.* (2021).
1055
1056 23. Giron, L.B. *et al.* Markers of fungal translocation are elevated during post-acute sequelae
1057 of SARS-CoV-2 and induce NF-κB signaling. *JCI Insight* **7** (2022).
1058
1059 24. Vijayakumar, B. *et al.* Immuno-proteomic profiling reveals aberrant immune cell
1060 regulation in the airways of individuals with ongoing post-COVD-19 respiratory disease.
1061 *Immunity* **0** (2022).
1062
1063 25. Schultheiß, C. *et al.* The IL-1β, IL-6, and TNF cytokine triad is associated with post-acute
1064 sequelae of COVID-19. *Cell Rep Med* **3**, 100663 (2022).
1065
1066 26. Littlefield, K.M. *et al.* SARS-CoV-2-specific T cells associate with inflammation and reduced
1067 lung function in pulmonary post-acute sequalae of SARS-CoV-2. *PLoS Pathog* **18**,
1068 e1010359 (2022).
1069
1070 27. Peluso, M.J., Thomas, I.J., Munter, S.E., Deeks, S.G. & Henrich, T.J. Lack of Antinuclear
1071 Antibodies in Convalescent Coronavirus Disease 2019 Patients With Persistent Symptoms.
1072 *Clinical Infectious Diseases* **74**, 2083-2084 (2022).
1073
1074 28. Bodansky, A. *et al.* Autoantigen profiling reveals a shared post-COVID signature in fully
1075 recovered and long COVID patients. *JCI Insight* **8** (2023).
1076

29. Muri, J. *et al.* Autoantibodies against chemokines post-SARS-CoV-2 infection correlate with disease course. *Nature immunology*, 1-8 (2023).

30. Files, J.K. *et al.* Duration of post-COVID-19 symptoms is associated with sustained SARS-CoV-2-specific immune responses. *JCI Insight* **6** (2021).

31. Peluso, M.J. *et al.* Long-term SARS-CoV-2-specific immune and inflammatory responses in individuals recovering from COVID-19 with and without post-acute symptoms. *Cell Rep* **36**, 109518 (2021).

32. Ma, T. *et al.* Protracted yet Coordinated Differentiation of Long-Lived SARS-CoV-2-Specific CD8(+) T Cells during Convalescence. *J Immunol* **207**, 1344-1356 (2021).

33. Neidleman, J. *et al.* SARS-CoV-2-Specific T Cells Exhibit Phenotypic Features of Helper Function, Lack of Terminal Differentiation, and High Proliferation Potential. *Cell Rep Med* **1**, 100081 (2020).

34. Neidleman, J. *et al.* Distinctive features of SARS-CoV-2-specific T cells predict recovery from severe COVID-19. *Cell Rep* **36**, 109414 (2021).

35. Neidleman, J. *et al.* mRNA vaccine-induced T cells respond identically to SARS-CoV-2 variants of concern but differ in longevity and homing properties depending on prior infection status. *Elife* **10** (2021).

36. Suryawanshi, R.K. *et al.* Limited cross-variant immunity from SARS-CoV-2 Omicron without vaccination. *Nature* **607**, 351-355 (2022).

37. Peluso, M.J. *et al.* Persistence, Magnitude, and Patterns of Postacute Symptoms and Quality of Life Following Onset of SARS-CoV-2 Infection: Cohort Description and Approaches for Measurement. *Open Forum Infect Dis* **9**, ofab640 (2022).

38. Rydyznski Moderbacher, C. *et al.* Antigen-Specific Adaptive Immunity to SARS-CoV-2 in Acute COVID-19 and Associations with Age and Disease Severity. *Cell* **183**, 996-1012 e1019 (2020).

39. Andersson, K.M. *et al.* Survivin co-ordinates formation of follicular T-cells acting in synergy with Bcl-6. *Oncotarget* **6**, 20043 (2015).

40. Thompson, R.C. *et al.* Molecular states during acute COVID-19 reveal distinct etiologies of long-term sequelae. *Nature Medicine*, 1-11 (2022).

41. Peluso, M.J. *et al.* Effect of oral nirmatrelvir on long COVID Symptoms: 4 cases and rationale for systematic studies. *Pathogens and Immunity* **7**, 95 (2022).

1121 42. Geng, L.N., Bonilla, H.F., Shafer, R.W., Miglis, M.G. & Yang, P.C. Case report of
1122 breakthrough long COVID and the use of nirmatrelvir-ritonavir. (2022).
1123
1124 43. Visvabharathy, L., Orban, Z.S. & Koralnik, I.J. Treatment of Long COVID with
1125 nirmatrelvir/ritonavir and tocilizumab in a patient with rheumatoid arthritis and SARS-
1126 CoV-2 antigen persistence: a case report. (2022).
1127
1128 44. Takahashi, T. *et al.* Sex differences in immune responses that underlie COVID-19 disease
1129 outcomes. *Nature* **588**, 315-320 (2020).
1130
1131 45. Sudre, C.H. *et al.* Attributes and predictors of long COVID. *Nature medicine* **27**, 626-631
1132 (2021).
1133
1134 46. Sparks, R. *et al.* Influenza vaccination reveals sex dimorphic imprints of prior mild COVID-
1135 19. *Nature*, 1-3 (2023).
1136
1137 47. Eddins, D.J. *et al.* Transcriptional reprogramming of infiltrating neutrophils drives lung
1138 disease in severe COVID-19 despite low viral load. *Blood Advances* (2022).
1139
1140 48. Ma, T. *et al.* Post-acute immunological and behavioral sequelae in mice after Omicron
1141 infection. *bioRxiv*, 2023.2006. 2005.543758 (2023).
1142
1143 49. Siewe, B., Nipper, A.J., Sohn, H., Stapleton, J.T. & Landay, A. FcRL4 expression identifies a
1144 pro-inflammatory B cell subset in viremic HIV-infected subjects. *Frontiers in immunology*
1145 **8**, 1339 (2017).
1146
1147 50. Durstenfeld, M.S. *et al.* Role of antibodies, inflammatory markers, and echocardiographic
1148 findings in post-acute cardiopulmonary symptoms after SARS-CoV-2 infection. *MedRxiv*
1149 (2021).
1150
1151 51. Peluso, M.J. *et al.* Plasma markers of neurologic injury and inflammation in people with
1152 self-reported neurologic postacute sequelae of SARS-CoV-2 infection. *Neurology-*
1153 *Neuroimmunology Neuroinflammation* **9** (2022).
1154
1155 52. Krishna, B.A. *et al.* Evidence of previous SARS-CoV-2 infection in seronegative patients
1156 with long COVID. *EBioMedicine* **81**, 104129 (2022).
1157
1158 53. Patel, H. *et al.* Proteomic blood profiling in mild, severe and critical COVID-19 patients.
1159 *Scientific reports* **11**, 1-12 (2021).
1160
1161 54. Bozorgmehr, N. *et al.* Galectin-9, a player in cytokine release syndrome and a surrogate
1162 diagnostic biomarker in SARS-CoV-2 infection. *MBio* **12**, e00384-00321 (2021).
1163

55. Du, L. *et al.* Human Galectin-9 Potently Enhances SARS-CoV-2 Replication and Inflammation in Airway Epithelial Cells (preprint). (2022).

56. Gardinassi, L.G., Souza, C.O., Sales-Campos, H. & Fonseca, S.G. Immune and metabolic signatures of COVID-19 revealed by transcriptomics data reuse. *Frontiers in immunology* **11**, 1636 (2020).

57. Su, W.-L. *et al.* Desaturation and heme elevation during COVID-19 infection: A potential prognostic factor of heme oxygenase-1. *Journal of Microbiology, Immunology and Infection* **54**, 113-116 (2021).

58. Hopp, M.T., Rathod, D.C. & Imhof, D. Host and viral proteins involved in SARS‐CoV‐2 infection differentially bind heme. *Protein Science* **31**, e4451 (2022).

59. Kronstein-Wiedemann, R. *et al.* SARS-CoV-2 Infects red blood cell progenitors and dysregulates hemoglobin and iron metabolism. *Stem Cell Reviews and Reports*, 1-13 (2022).

60. Lechuga, G.C. *et al.* SARS-CoV-2 proteins bind to hemoglobin and its metabolites. *International Journal of Molecular Sciences* **22**, 9035 (2021).

61. Grobbelaar, L.M. *et al.* Relative hypercoagulopathy of the SARS-CoV-2 beta and delta variants when compared to the less severe omicron variants is related to TEG parameters, the extent of fibrin amyloid microclots, and the severity of clinical illness. Seminars in thrombosis and hemostasis; 2022: Thieme Medical Publishers, Inc.; 2022.

62. Kruger, A. *et al.* Proteomics of fibrin amyloid microclots in long COVID/post-acute sequelae of COVID-19 (PASC) shows many entrapped pro-inflammatory molecules that may also contribute to a failed fibrinolytic system. *Cardiovascular Diabetology* **21**, 1-23 (2022).

63. Kell, D.B., Laubscher, G.J. & Pretorius, E. A central role for amyloid fibrin microclots in long COVID/PASC: origins and therapeutic implications. *Biochemical Journal* **479**, 537-559 (2022).

64. George, A.F. *et al.* Deep Phenotypic Analysis of Blood and Lymphoid T and NK Cells From HIV+ Controllers and ART-Suppressed Individuals. *Front Immunol* **13**, 803417 (2022).

65. Neidleman, J. *et al.* Phenotypic analysis of the unstimulated in vivo HIV CD4 T cell reservoir. *Elife* **9**, e60933 (2020).

66. Tsampasian, V. *et al.* Risk Factors Associated With Post-COVID-19 Condition: A Systematic Review and Meta-analysis. *JAMA Intern Med* (2023).

1208 67. Ferretti, A.P. *et al.* Unbiased Screens Show CD8(+) T Cells of COVID-19 Patients Recognize
1209 Shared Epitopes in SARS-CoV-2 that Largely Reside outside the Spike Protein. *Immunity*
1210 **53**, 1095-1107 e1093 (2020).
1211
1212 68. Costantini, A. *et al.* Effects of cryopreservation on lymphocyte immunophenotype and
1213 function. *Journal of immunological methods* **278**, 145-155 (2003).
1214
1215 69. Cavrois, M. *et al.* Mass cytometric analysis of HIV entry, replication, and remodeling in
1216 tissue CD4+ T cells. *Cell reports* **20**, 984-998 (2017).
1217
1218 70. Steiner, S. *et al.* SARS-CoV-2 T Cell Response in Severe and Fatal COVID-19 in Primary
1219 Antibody Deficiency Patients Without Specific Humoral Immunity. *Front Immunol* **13**,
1220 840126 (2022).
1221
1222 71. Roederer, M., Nozzi, J.L. & Nason, M.C. SPICE: exploration and analysis of post-cytometric
1223 complex multivariate datasets. *Cytometry A* **79**, 167-174 (2011).
1224
1225 72. Hao, Y. *et al.* Integrated analysis of multimodal single-cell data. *Cell* **184**, 3573-3587 e3529
1226 (2021).
1227
1228 73. Korsunsky, I. *et al.* Fast, sensitive and accurate integration of single-cell data with
1229 Harmony. *Nat Methods* **16**, 1289-1296 (2019).
1230
1231 74. Breiman, L. Random forests. *Machine learning* **45**, 5-32 (2001).
1232
1233 75. Bates, D., Mächler, M., Bolker, B. & Walker, S. Fitting linear mixed-effects models using
1234 lme4. *arXiv preprint arXiv:1406.5823* (2014).
1235
1236 76. Lenth, R., Singmann, H., Love, J., Buerkner, P. & Herve, M. Emmeans: Estimated marginal
1237 means, aka least-squares means. *R package version* **1**, 3 (2018).
1238
1239 77. Dobin, A. *et al.* STAR: ultrafast universal RNA-seq aligner. *Bioinformatics* **29**, 15-21 (2013).
1240
1241 78. Love, M.I., Huber, W. & Anders, S. Moderated estimation of fold change and dispersion
1242 for RNA-seq data with DESeq2. *Genome biology* **15**, 1-21 (2014).
1243
1244 79. Vvan der Laan, M. & Pollard, K. Hybrid clustering of gene expression data with
1245 visualization and the bootstrap. *Journal of Statistical Planning and Inference* **117**, 275-303
1246 (2003).
1247
1248 80. Zheng, G.X. *et al.* Massively parallel digital transcriptional profiling of single cells. *Nature*
1249 *communications* **8**, 14049 (2017).
1250

1251 81. Ahlmann-Eltze, C. & Huber, W. glmGamPoi: fitting Gamma-Poisson generalized linear
1252 models on single cell count data. *Bioinformatics* **36**, 5701-5702 (2020).
1253
1254 82. Blondel, V.D., Guillaume, J.-L., Lambiotte, R. & Lefebvre, E. Fast unfolding of communities
1255 in large networks. *Journal of statistical mechanics: theory and experiment* **2008**, P10008
1256 (2008).
1257
1258 83. McGinnis, C.S. *et al.* No detectable alloreactive transcriptional responses under standard
1259 sample preparation conditions during donor-multiplexed single-cell RNA sequencing of
1260 peripheral blood mononuclear cells. *BMC biology* **19**, 1-11 (2021).
1261
1262 84. Xu, C. *et al.* Comprehensive multi-omics single-cell data integration reveals greater
1263 heterogeneity in the human immune system. *Iscience* **25**, 105123 (2022).
1264
1265 85. Ianevski, A., Giri, A.K. & Aittokallio, T. Fully-automated and ultra-fast cell-type
1266 identification using specific marker combinations from single-cell transcriptomic data.
1267 *Nature communications* **13**, 1246 (2022).
1268
1269 86. Robinson, M.D., McCarthy, D.J. & Smyth, G.K. edgeR: a Bioconductor package for
1270 differential expression analysis of digital gene expression data. *bioinformatics* **26**, 139-
1271 140 (2010).
1272
1273 87. Holm, S. A simple sequentially rejective multiple test procedure. *Scandinavian journal of*
1274 *statistics*, 65-70 (1979).
1275
1276 88. Benjamini, Y. & Hochberg, Y. Controlling the false discovery rate: a practical and powerful
1277 approach to multiple testing. *Journal of the Royal statistical society: series B*
1278 *(Methodological)* **57**, 289-300 (1995).
1279
1280 89. Crowell H, Germain P, Soneson C, Sonrel A & M, R. muscat: Multi-sample multi-group
1281 scRNA-seq data analysis tools. https://doi.org/10.18129/B9.bioc.muscat, R package
1282 version 1.14.10 (2023).
1283
1284 90. Assarsson, E. *et al.* Homogenous 96-plex PEA immunoassay exhibiting high sensitivity,
1285 specificity, and excellent scalability. *PloS one* **9**, e95192 (2014).
1286
1287 91. Bäckryd, E., Tanum, L., Lind, A.-L., Larsson, A. & Gordh, T. Evidence of both systemic
1288 inflammation and neuroinflammation in fibromyalgia patients, as assessed by a multiplex
1289 protein panel applied to the cerebrospinal fluid and to plasma. *Journal of pain research*
1290 **10**, 515 (2017).
1291
1292 92. Björkesten, J. *et al.* Stability of proteins in dried blood spot biobanks. *Molecular & Cellular*
1293 *Proteomics* **16**, 1286-1296 (2017).
1294

1295 93. Wigren, M. *et al.* Decreased levels of stem cell factor in subjects with incident coronary
1296 events. *Journal of internal medicine* **279**, 180-191 (2016).
1297
1298 94. Loskog, A. *et al.* Immunostimulatory AdCD40L gene therapy combined with low-dose
1299 cyclophosphamide in metastatic melanoma patients. *British journal of cancer* **114**, 872-
1300 880 (2016).
1301
1302 95. Kolde, R. & Kolde, M.R. Package 'pheatmap'. *R package* **1** (2018).
1303
1304 96. Doncheva, N.T., Morris, J.H., Gorodkin, J. & Jensen, L.J. Cytoscape StringApp: network
1305 analysis and visualization of proteomics data. *Journal of proteome research* **18**, 623-632
1306 (2018).
1307
1308 97. Shannon, P. *et al.* Cytoscape: a software environment for integrated models of
1309 biomolecular interaction networks. *Genome research* **13**, 2498-2504 (2003).
1310
1311 98. Organization, W.H. A clinical case definition of post COVID-19 condition by a Delphi
1312 consensus, 6 October 2021. *WHO/2019-nCoV/Post_COVID-*
1313 *19_condition/Clinical_case_definition/2021.1* (2021).
1314
1315

FIGURE LEGENDS

Fig. 1. Study Design. Schematic of experimental design and data analyses. Plasma and sera from 27 individuals with Long COVID (LC) and 16 individuals without LC (Non-LC) were subjected to Olink and serological analyses. PBMCs from the same individuals were subjected to RNAseq/scRNAseq analysis, as well as to CyTOF analysis at baseline, or following a 6-hour stimulation with peptides derived from SARS-CoV-2 spike proteins (see Methods) to analyze T cell responses. The cells for CyTOF were treated with viability marker, fixed, and stained with a 39-parameter panel (Table S2) prior to analysis on a CyTOF instrument. The indicated tools on the right were then used for analyses of the resulting high-dimensional datasets.

Fig. 2. Identification and characterization of SARS-CoV-2-specific T cells in individuals from the LIINC cohort. A. SARS-CoV-2-specific CD4+ T cells can be identified as those producing IFNγ, TNFα, or IL2 in response to SARS-CoV-2 peptide stimulation. Cells were analyzed by intracellular cytokine staining in the absence (*top row*) or presence (*bottom row*) of SARS-CoV-2 peptides. **B.** SARS-CoV-2-specific CD8+ T cells can be identified as those producing IFNγ, TNFα, or MIP1β in response to SARS-CoV-2 peptide stimulation. Cells were analyzed by intracellular cytokine staining in the absence (*top row*) or presence (*bottom row*) of SARS-CoV-2 peptides. **C, D.** No significant differences in the magnitude of the T cell responses were observed between LC and non-LC individuals within the CD4+ (**C**) or CD8+ (**D**) T cell compartments (student's t-tests). **E.** Analysis of polyfunctionality of SARS-CoV-2-specific CD4+ T cells. SPICE analysis revealed that polyfunctional SARS-CoV-2-specific CD4+ T cells co-expressing IFNγ, IL2, and TNFα (*category 1*) trended higher in non-LC than LC individuals albeit insignificantly (permutation test). TNFα single positive cells (*category 7*) made up the vast majority of SARS-CoV-2-specific CD4+ T cells in both LC and non-LC individuals. **F.** Analysis of polyfunctionality of SARS-CoV-2-specific CD8+ T cells. SPICE analysis revealed that polyfunctional SARS-CoV-2-specific CD8+ T cells co-expressing IFNγ, MIP1β, and TNFα (*category 1*) trended higher in non-LC than LC individuals albeit insignificantly (permutation test). TNFα single positive cells (*category 7*) made up the majority of SARS-CoV-2-specific CD8+ T cells in both LC and non-LC individuals, but to a lesser extent than for SARS-CoV-2-specific CD4+ T cells. Relative to SARS-CoV-2-specific CD4+ T cells, SARS-CoV-2-specific CD8+ T cells more frequently produced IFNγ.

Fig 3. Tcm, Tfh, and Treg frequencies differ between LC and Non-LC individuals. A. CD4+ T cell subset analysis reveals higher proportions of Tcm, Tfh, and Treg in LC vs. non-LC individuals. **$p<0.01$, *$p<0.05$ (student's t-test). **B.** No significant differences were observed in the proportion of the indicated SARS-CoV-2-specific CD4+ T cell subsets between LC vs. non-LC individuals. Phenotypic definition of subsets were as follows: naïve T cells (Tn): CD45RA+CD45RO-CCR7+CD95-, stem cell memory T cells (Tscm): CD45RA+CD45RO-CCR7+CD95+, central memory T cells (Tcm): CD45RA-CD45RO+CCR7+CD27+, effector memory T cells (Tem): CD45RA-CD45RO+CCR7-CD27-, transitional memory T cells (Ttm): CD45RA-CD45RO+CCR7-CD27+, effector memory RA T cells (Temra): CD45RA+CD45RO-CCR7-, T follicular helper cells (Tfh): CD45RA-CD45RO+PD1+CXCR5+, and regulatory T cells (Treg): CD45RA-CD45RO+CD127-CD25+.

Fig. 4. SARS-CoV-2-specific CD4+ T cells from individuals with LC preferentially express homing receptors associated with migration to inflamed tissues. A. tSNE contour depiction of SARS-CoV-2-specific CD4+ T cells from LC and non-LC individuals, highlighting different distribution of cells from the two groups. **B.** Expression of the chemokine receptors CXCR4, CXCR5, and CCR6 are elevated in SARS-CoV-2-specific CD4+ T cells from LC as compared to non-LC individuals. MSI corresponds to mean signal intensity of the indicated markers' expression

level, reported as arcsinh-transformed CyTOF data as detailed in the Methods. **C, D.** CXCR4+CXCR5+ and CXCR5+CCR6+ SARS-CoV-2-specific ***(C)*** and total ***(D)*** CD4+ T cells are significantly elevated in LC as compared to non-LC individuals, while their CXCR4+CCR6+ counterparts trended higher in the LC group. *p<0.05 (student's t-test). **E**. The frequencies of CXCR4+CXCR5+ and CXCR5+CCR6+ CD4+ T cells are significantly positively associated (p<0.0001 for CXCR4+CXCR5+, p<0.001 for CXCR5+CCR6+) with the frequencies of Tfh in LC, but not non-LC, individuals. **F**. The frequencies of SARS-CoV-2-specific CXCR4+CXCR5+ and CXCR5+CCR6+ CD4+ T cells are significantly positively associated (p<0.0001 for CXCR4+CXCR5+, p<0.0001 for CXCR5+CCR6+) with the frequencies of SARS-CoV-2-specific Tfh in LC, but not non-LC, individuals. In *panels E-F*, correlation estimates were identified as R values (Pearson correlation coefficients).

Fig. 5. SARS-CoV-2-specific CD8+ T cells from individuals with LC preferentially express exhaustion markers PD1 and CTLA4. A. tSNE contour depiction of SARS-CoV-2-specific CD8+ T cells from LC and non-LC individuals, highlighting different distribution of cells from the two groups. **B.** Expression of exhaustion markers PD1 and CTLA4, but not TIGIT, are elevated on SARS-CoV-2-specific CD8+ T cells from LC as compared to non-LC individuals. MSI corresponds to mean signal intensity of the indicated markers' expression level. **C, D.** PD1+CTLA4+ cells are significantly enriched among SARS-CoV-2-specific CD8+ T cells (**C**) but not total CD8+ T cells (**D**) in LC as compared to non-LC individuals. By contrast, TIGIT+CTLA4+ and PD1+TIGIT+ total and SARS-CoV-2-specific CD8+ T cells were equivalently distributed between LC and non-LC individuals. *p<0.05 (student's t-test).

Fig. 6. Dis-coordinated humoral and adaptive immunity in individuals with LC. A. SARS-CoV-2 spike RBD antibody levels are elevated in LC as compared to non-LC individuals. *p<0.05 (student's t-test). **B.** Individuals with LC harboring the highest humoral response (green oval) are not those exhibiting highest levels of exhausted PD1+CTLA4+ SARS-CoV-2-specific CD8+ T cells (purple oval). **C**. Frequencies of PD1+CTLA4+ SARS-CoV-2-specific CD8+ T cells and SARS-CoV-2-specific CD4+ Treg cells are negatively associated only in individuals with LC. **D-F.** SARS-CoV-2 spike RBD antibody levels are significantly positively associated with the frequencies of SARS-CoV-2-specific CD4+ T cells ***(D)***, SARS-CoV-2-specific Tfh ***(E)***, and SARS-CoV-2-specific CD8+ T cells ***(F)*** in non-LC individuals, but not in individuals with LC. In *panels D-F*, the correlation estimates (identified as R in the figures) for the non-LC group were significantly (p<0.05 for the CD4+ T cells, p<0.01 for Tfh cells, p<0.001 for the CD8+ T cells) different from zero while the corresponding estimates were n.s. (p>0.05) for the LC group (Pearson r t-tests).

Fig. 7. Global differential gene and gene product expression in participants with and without LC. **A.** Relative gene expression levels of top two significantly differentially expressed genes (DEGs) from bulk RNAseq analysis of LC vs. non-LC individuals. OR7D2 corresponds to Olfactory Receptor family 7D2 ($\log_2$ fold-change=3.63), and ALAS2 to 5'Aminolevulinate Synthase 2 ($\log_2$ fold-change=2.58). *p < 0.05 (Wald test, with Benjamini-Hochberg correction). Purple asterisks identify the female donors selected for follow-up scRNAseq analyses. **B.** Clustered heatmap of the top 50 DEGs in PBMCs in LC compared to non-LC individuals. Genes are grouped into k-clusters based on similarity. Note four modules of gene expression, with the second corresponding to immunoglobulin and T cell genes (under-expressed in LC), and the third corresponding to heme synthesis and carbon dioxide transport (over-expressed in LC). **C.** Network mapping of related DEGs from bulk RNAseq analysis. Each node corresponds to a gene, and colors of nodes indicate the extent of change as indicated in the heatmap scale bar, with red corresponding to upregulation in individuals with LC, and blue corresponding to downregulation in individuals with LC. Edges depict the functional relevance between pairs of genes, where the thickness of the edge corresponds to the confidence of the evidence. The highly networked nature

of the indicated genes supports their association with LC. **D.** UMAP of annotated clusters from samples analyzed by scRNAseq. **E.** Both OR7D2 and ALAS2 are broadly expressed among PBMC subsets of individuals with LC. Shown are UMAP depictions of cells expressing (*blue*) or not expressing (*grey*) OR7D2 or ALAS2 as indicated. **F.** Clustered heatmap of the top 25 differentially expressed plasma proteins from Olink Proximity Extension Assay with markers grouped into k-clusters based on similarity. Note a dominant module of inflammatory-related genes including LGALS9, CCL21, CCL22, TNF, CXCL10, and CD48. **G.** Network mapping of related differentially expressed proteins as detected by Olink. Graph representations are as described in *panel C*. Note the simultaneous over-expression of IL4 and CCL22 (in red) with under-expression of IL5 (in blue), all three proteins of which are involved in Th2 immune responses.

Fig. S1. Clinical characteristics of LC and non-LC individuals analyzed in this study. A. Strategy of biospecimen selection for study. Individuals demonstrate variable recovery following COVID-19, with many experiencing symptom resolution within 4 months (typically <30 days) in a manner that is sustained (solid blue line). However, some experience symptoms that persist (solid red line). Symptoms can also newly develop (dotted red line) or diminish (dotted blue line) over time. Per WHO definition, symptoms persisting beyond 3 months post-infection are defined as LC [98]. In order to minimize the effects of between-individual heterogeneity, we selected individuals demonstrating a consistent post-acute phenotype (LC or Non-LC) at two timepoints timed 4 and 8 months following initial SARS-CoV-2 infection, and performed biologic measurements on samples from the 8-month timepoint. All samples were collected and cryopreserved prior to the individuals ever receiving a SARS-CoV-2 vaccine or experiencing a clinically detected reinfection. **B.** Sex distribution of individuals from the LIINC cohort analyzed in this study. Overall, 55.8% of the participants were female; the non-LC group comprised 43.75% females and the LC group 62.96% females. **C.** The proportion of LC and non-LC individuals that were hospitalized at the time of acute COVID-19 infection. Overall, 20.9% of the participants were hospitalized: 12.5% among the non-LC individuals, and 25.9% among the individuals with LC. **D.** The number of sequelae symptoms among the individuals with LC. Number of sequelae symptoms at four (M4) and eight (M8) months are shown. *$p<0.05$ (paired sample t-test). **E**. Most individuals in the cohort did not exhibit comorbidities. The proportion of LC and non-LC individuals that exhibited the indicated comorbidities are indicated. **F**. Individuals with LC had significantly higher BMI than individuals without LC in the cohort. *$p<0.05$ (student's t-test).

Fig. S2. Cytokine and effector molecule expression on T cells in the absence or presence of SARS-CoV-2 peptides. A-B. Gating strategy to identify T cell populations. Intact, live, singlet cells from a baseline (unstimulated) ***(A)*** or SARS-CoV-2 peptide-treated ***(B)*** samples were gated for T cells (CD3+) followed by sub-gating on CD4+ and CD8+ T cells as indicated. **B.** CD4+ T cells from a representative donor, in the absence or presence of SARS-CoV-2 peptides. The red box highlights the three cytokines used to define SARS-CoV-2-specific CD4+ T cells. **C.** CD8+ T cells from a representative donor, in the absence or presence of SARS-CoV-2 peptides. The red boxes highlight the three cytokines used to define SARS-CoV-2-specific CD8+ T cells.

Fig. S3. SARS-CoV-2-specific T cell responses defined individually as those producing IFNγ, IL2, TNFα, and MIP1β do not differ between LC and non-LC individuals. A. Shown are the proportions of SARS-CoV-2-specific CD4+ T cells as defined by cells producing IFNγ, IL2, or TNFα in response to SARS-CoV-2 peptide stimulation. n.s.: non-significant as determined by student's t-test. **B.** Shown are the proportions of SARS-CoV-2-specific CD8+ T cells as defined by cells producing IFNγ, MIP1β, or TNFα in response to SARS-CoV-2 peptide stimulation. n.s.: non-significant as determined by student's t-test. **C.** IL6-producing CD4+ T cells are observed

after SARS-CoV-2 peptide stimulation in some donors. Shown are cells from a representative individual with LC. **D.** IL6+ SARS-CoV-2-specific CD4+ T cells are exclusively observed from participants with LC. *p<0.05 (Welch's t-test). Results in panels *C* and *D* were pre-gated on live, singlet CD4+ T cells.

Fig. S4. Gating strategy to define classical T cell subsets. Shown are gating strategies to define the indicated subsets of CD4+ (**A**) and CD8+ (**B**) T cells.

Fig. S5. Subset distribution of total and SARS-CoV-2-specific CD8+ T cells among LC and Non-LC individuals. A. Tem frequencies trended higher among total CD8+ T cells from LC as compared to non-LC individuals (student's t-test). **B.** Temra frequencies trended lower among SARS-CoV-2-specific CD8+ T cells from LC as compared to non-LC individuals (student's t-test).

Fig. S6. MSI of all CyTOF phenotyping markers among CD4+ T cells from individuals with and without LC. Antigens are shown in the order listed in Table S2. Results are gated on live, singlet CD4+ T cells. No significant differences were observed between LC and non-LC individuals for any of the antigens (t-test with multiple correction by Sidak adjustment).

Fig. S7. MSI of all CyTOF phenotyping markers among CD8+ T cells from individuals with and without LC. Results are similar to that shown in Fig. S6, but gated on CD8+ T cells. No significant differences were observed between LC and non-LC individuals for any of the antigens (t-test with multiple correction by Sidak adjustment).

Fig. S8. MSI of all CyTOF phenotyping markers among SARS-CoV-2-specific CD4+ T cells from individuals with and without LC. Results are similar to that shown in Fig. S6, but gated on SARS-CoV-2-specific CD4+ T cells. No significant differences were observed between LC and non-LC individuals for any of the antigens (t-test with multiple correction by Sidak adjustment).

Fig. S9. MSI of all CyTOF phenotyping markers among SARS-CoV-2-specific CD4+ T cells from individuals with and without LC. Results are similar to that shown in Fig. S6, but gated on SARS-CoV-2-specific CD8+ T cells. No significant differences were observed between LC and non-LC individuals for any of the antigens (t-test with multiple correction by Sidak adjustment).

Fig. S10. Activated T cells are not more abundant in individuals with LC. The percentages of total CD4+ T cells **(A)**, total CD8+ T cells **(B)**, SARS-CoV-2-specific CD4+ T cells **(C)**, and SARS-CoV-2-specific CD8+ T cells **(D)** expressing acute activation markers CD38, HLADR, and Ki67 were not significantly different between individuals with and without LC. Shown are proportions of cells expressing each of these respective markers (first three columns), or co-expressing all three of these markers (last column). n.s. = non-significant as determined by student's t-tests.

Fig. S11. Sex-dimorphic CD4+ T cell cluster distribution in individuals with LC. A. Cluster distribution among baseline CD4+ T cells as depicted by UMAP. **B.** Female individuals with LC harbor significantly lower frequencies (raw p-value = 0.03, FDR = 0.19) of cluster A1 cells relative to female non-LC individuals, and male individuals with LC harbor significantly lower frequencies (raw p-value = 0.02, FDR = 0.19) of cluster A4 cells relative to male non-LC individuals. P-values were derived from a GLMM fit (see Methods). Individual points represent the % of all cells from a given participant that belong to clusters A1 or A4. **C.** Relative to total CD4+ T cells, cluster A1 is characterized by expression of naïve cell markers ($CD45RA^{high}CD45RO^{low}CD27^{high}$), and low expression of inflammatory tissue homing receptors ($CD29^{low}CXCR4^{low}$) but high expression lymph node homing receptors ($CD62L^{high}CCR7^{high}$). The activation markers HLA-DR and OX40

were also lowly expressed in cluster A1 cells. **D.** Relative to total CD4+ T cells, cluster A4 is characterized by expression of terminally differentiated effector memory T cell markers ($CD45RA^{low}CD45RO^{high}CD27^{low}CCR7^{low}CD57^{high}$), and high expression of homing receptors for inflamed tissues ($CD29^{high}CXCR4^{high}CCR5^{high}$) but low expression of lymph node homing receptors ($CD62L^{low}CCR7^{low}$). The cytolysis-associated markers perforin, granzyme, and LAMP1 were expressed at elevated levels in cluster A4 cells. ****p<0.0001 (paired t-test). For panels *C* and *D*, data are depicted as histograms showing distribution of marker expression among all participants, or as bar graphs depicting the distribution of the MSI of each marker within each individual participant. Comparisons are shown between cells belonging to the indicated cluster as compared to total CD4+ T cells.

Fig. S12. Sex-dimorphic differential CD8+ T cell cluster distribution in individuals with LC. A. Cluster distribution among baseline CD8+ T cells as depicted by UMAP. **B.** Female individuals with LC harbor significantly lower frequencies (raw p-value = 0.046, FDR = 0.22) of cluster B1 cells and significantly higher frequencies (p-value = 0.024, FDR = 0.22) of cluster B2 cells, relative to female non-LC individuals. P-values were derived from a GLMM fit (see Methods). Individual points represent the % of all cells from a given participant that belong to clusters B1 or B2. **C.** Relative to total CD8+ T cells, cluster B1 is characterized by expression of naïve cell markers ($CD45RA^{high}CD45RO^{low}CD27^{high}$), and low expression of tissue homing receptors ($CD29^{low}CXCR4^{low}$) but high expression lymph node homing receptors ($CD62L^{high}CCR7^{high}$). The activation markers HLA-DR and OX40 were also lowly expressed in cluster B1 cells. **D.** Relative to total CD8+ T cells, cluster B2 is characterized by expression of terminally differentiated effector memory T cell markers ($CD45RA^{low}CD45RO^{high}CD27^{low}CCR7^{low}CD57^{high}$), and high expression of homing receptors for inflamed tissues ($CD29^{high}CXCR4^{high}CCR5^{high}$) but low expression of lymph node homing receptors ($CD62L^{low}CCR7^{low}$). The cytolysis markers perforin, granzyme, and LAMP1 were expressed at elevated levels in cluster B2 cells. ****p<0.0001 (paired t-test). For panels *C* and *D*, data are depicted as histograms showing distribution of marker expression among all participants, or as bar graphs depicting the distribution of the MSI of each marker within each individual participant. Comparisons are shown between cells belonging to indicated cluster as compared to total CD8+ T cells.

Fig. S13. FACS validation that CD4+ T cells from individuals with LC preferentially express CXCR4, CXCR5, and CCR6. A. Expression levels of CXCR4, CXCR5, and CCR6 as assessed by FACS significantly correlates with those as assessed by CyTOF. FACS data were reported as mean fluorescence intensity (MFI), while CyTOF data were reported as mean signal intensity (MSI). CyTOF data were arcsinh-transformed, while FACS data were arcsinh-scaled. Correlation estimates were identified as R values (Pearson correlation coefficients). **B.** FACS gating strategy to identify memory CD4+ T cells expressing various combinations of CXCR4, CXCR5, and CCR6. **C.** CXCR4+CXCR5+, CXCR5+CCR6+, and CXCR4+CCR6+ CD4+ T cells are significantly elevated in LC as compared to non-LC individuals. *p<0.05 (student's t-test).

Fig. S14. FACS validation that SARS-CoV-2-specific CD8+ T cells from individuals with LC preferentially express exhaustion markers PD1 and CTLA4. FACS analysis demonstrating that SARS-CoV-2-specific CD8+ T cells co-expressing PD1 and CTLA4 were elevated in individuals with LC, while total PD1+CTLA4+ CD8+ T cells were not. *p<0.05 (student's t-test). Note that in these FACS experiments, SARS-CoV-2-specific CD8+ T cells were defined as those specifically inducing IFNγ and/or TNFα in response to SARS-CoV-2 peptide stimulation, while those in the CyTOF experiments (Fig. 5) were defined as those specifically inducing IFNγ, TNFα, and/or MIP1β. The difference was because MIP1β antibody exhibited background staining in FACS and could not be used to define SARS-CoV-2-specific T cells.

Fig. S15. Global differential gene and gene product expression in participants with and without LC. **A.** Heatmap of the top 50 DEGs in PBMCs in LC compared to non-LC individuals. Note data are the same as those depicted in Fig. 7B, but separated by LC vs. non-LC status. **B.** Clustered heatmap of the top 25 differentially expressed plasma proteins from Olink Proximity Extension Assay. Note data are the same as those depicted in Fig. 7F, but separated by LC vs. non-LC status.

Fig. S16. scRNAseq analysis of reveals OR7D2 and ALAS2 expression in multiple subsets of immune cells from individuals with LC. A, B. UMAP of cells from LC (n=8) vs. non-LC (n=4) individuals ***(A)***, and among the LC individuals those classified as OR7D2^{high} (n=4) vs. ALAS2^{high} (n=4) ***(B)***, revealing lack of profound global differences in gene expression between any of these groups. **C.** OR7D2 expression is highest in the OR7D2^{high} LC group, and ALAS2 expression is highest in the ALAS2^{high} LC group. **D.** OR7D2 and ALAS2 are broadly expressed by multiple PBMC subsets in individuals with LC. Shown are the mean % of cells that were positive for OR7D2 or ALAS2 reads, grouped by cellular clusters defined in Fig. 7D. Note that both OR7D2 and ALAS2 transcripts were detected in all clusters except 9 and 10. OR7D2 was most highly expressed in Cluster 3 (monocytes), while ALAS2 was most highly expressed in Cluster 8 (B cells), with Cluster 5 (CD8+ T cells) and Clusters 0/7 (CD4+ T cells) also being relatively high expressors. **E, F.** Among all clusters expressing ORD72 or ALAS2, OR7D2 was preferentially expressed in the OR7D2^{high} LC group ***(E)*** while ALAS2 was preferentially expressed in the ALAS2^{high} LC group ***(F)***. *p<0.05, **p<0.01, as determined by two-sample Welch t-tests, followed by multiple testing correction (across 3 pairwise combinations) using the Holm procedure.

Fig. S17. Opposite associations of IL4 levels with T cells expressing inflammatory chemokine receptors in individuals with vs. without LC. (**A**) The percentages of CXCR4+CXCR5+ CD4+ T cells are significantly positively associated with IL4 levels in individuals with LC (p<0.05), while these parameters negatively associate in individuals without LC (p<0.05). (**B**) The percentages of CXCR5+CCR6+ CD4+ T cells are significantly positively associated with IL4 levels in individuals with LC (p<0.05), while these parameters negatively associate in individuals without LC (p<0.01). Correlation estimates were defined as R values in the figures, and significance was determined using Pearson r t-tests.

Fig. S18. Validation of CyTOF antibodies. (**A**) Validation of CyTOF detection of antigens through analysis of expression patterns on tonsillar T cells and B cells. Most cells from the human lymphoid aggregate cultures generated from tonsils correspond to T cells and B cells [69]. Therefore, as demonstrated in the schematic on the bottom, visualizing CD3 on the y-axis allows differentiation of T cells (top population) from B cells (bottom population). The expression patterns of the indicated antigens on T and B cells are similar to those previously reported and validated [69]. (**B**) Validation of CyTOF detection of effector molecule expression was performed by using PBMCs stimulated with PMA/ionomycin or LPS (see Methods). As demonstrated in the schematic, visualizing CD3 on the y-axis allows differentiation of T cells (top population) from other immune subsets including monocytes and other innate immune cells. The expression patterns of the shown effectors are as expected and consistent prior studies [32, 33, 34, 35]. (**C**) Validation of Treg gating. Compared to naïve CD4+ T cells (Tn: CD3+CD4+CD45RO-CD45RA+CCR7+CD95-), the Treg population (defined as CD3+CD4+CD45RO+CD45RA-CD25+CD127-) expressed significantly higher levels of the Treg lineage marker Foxp3, thereby validating their Treg identity. ****p<0.0001 (paired t-test). (**D**) CyTOF detection of CD30 and Ki67 were validated by demonstrating that memory CD4+ T cells (Tm: CD3+CD4+CD45RO+CD45RA-) expressed significantly higher levels of these markers as compared to naïve CD4+ T cells, as expected. ****p<0.0001 (paired t-test). (**E**) Illustration of Tfh gate on PBMC samples used for validation. Cells were pre-gated on memory CD4+ T cells.

TABLES

Table 1: Participants' sequelae status at the 8th-month visit

Status	N	Age[1]	M4[2]	M8[3]	Male	Female	Hos[4]	Non-Hos[5]
LC	27	46	4.5	7	10	17	7	20
Non-LC	16	45.5	0	0	9	7	2	14

Age[1]: Median age of participants involved in this study.
M4[2]: Median symptom counts at the 4th-month visit.
M8[3]: Median symptom counts at the 8th-month visit.
Hos[4]: Participants were hospitalized at the time of acute COVID-19.
Non-Hos[5]: Outpatient participants who were not hospitalized for COVID-19.

Table 2: Detailed participants' demographics and hospitalization status at the 8th-month visit

Participants	**All**	**Sex**		**Hospitalized**	
		Male	Female	Yes	No
N	43	19	24	9	34
Age (Median)	46	53	43	46	48
M4[1] (Median)	2.5	0	5	7	2
M8[2] (Median)	5	2	7	10	3
Female	24	-	-	6	18
Hospitalized	9	3	6	-	-
Race (N)					
White	25	13	12	0	25
Latinx*	11	6	5	7	4
Black	2	2	0	1	1
Asian	3	1	2	1	2
NA#	2	2	0	0	2

M4[1]: Symptom counts at the 4th-month visit.
M8[2]: Symptom counts at the 8th-month visit.
Latinx*: Hispanic or Latino.
NA#: Data are not available here.

Table S1: Participants from the LIINC cohort

Person ID	**Age**	**Race**	**Status**	**Sex**	**Hospitalized**
4107	40	White	LC	Female	No
4111	49	White	Non-LC	Female	No
5018	31	White	Non-LC	Female	No

5019*	37	White	Non-LC	Female	No
5024*	43	White	Non-LC	Female	No
5027*	38	NA	Non-LC	Female	No
5030	59	White	Non-LC	Male	No
5035	40	White	Non-LC	Male	No
5036	19	White	LC	Female	No
5044	40	AA	Non-LC	Female	No
5048	48	Asian	Non-LC	Male	No
5049	71	Asian	LC	Male	No
5053	60	White	Non-LC	Male	No
5054	31	Latinx	LC	Male	No
5055	67	White	LC	Male	No
5057^	57	White	LC	Female	No
5076	40	White	LC	Male	No
5080	34	Latinx	LC	Female	Yes
5081	51	Latinx	LC	Female	No
5082	52	Latinx	Non-LC	Male	Yes
5088&	43	AA	LC	Female	Yes
5089^	46	Latinx	LC	Female	Yes
5091	25	Latinx	LC	Male	Yes
5092	43	White	LC	Female	No
5103	53	Latinx	Non-LC	Male	Yes
5120	68	White	Non-LC	Male	No
5122	44	Asian	LC	Female	Yes
5132	66	White	LC	Male	No
5133	71	White	LC	Female	No
5134	65	Latinx	LC	Male	No
5139&	48	White	LC	Female	No
5142	48	White	LC	Male	No
5144&	26	White	LC	Female	No
5148	52	White	LC	Female	No
5186^	49	Latinx	LC	Female	Yes
5205	59	White	LC	Male	No
5206*	50	White	Non-LC	Female	No
5219	42	White	Non-LC	Male	No
5221	32	White	Non-LC	Male	No
5222	54	White	LC	Male	No
5247&	46	Latinx	LC	Female	Yes
5250	43	NA	LC	Female	No
5257^	33	Latinx	LC	Female	No

Latinx: Hispanic or Latino.
AA: Black or African American.
NA: Not available.
*Analyzed by scRNAseq (non-LC group)
&Analyzed by scRNAseq (OR7D2^{high} LC group)

1652 ^ Analyzed by scRNAseq (ALAS2^{high} LC group)
1653
1654 **Table S2: CyTOF antibodies used in study**
1655

Antibody	Clone	Catalog	Metal	Manufacturer
CD196/CCR6	11A9	3141014A	141Pr	Standard BioTools
IL4*	MP4-25D2	3142002B	142Nd	Standard BioTools
CD38	HIT2	303535	143Nd	BioLegend
CD195/CCR5	NP6G4	3144007A	144Nd	Standard BioTools
CD30	BerH8	555827	145Nd	BD
CD8α	RPAT8	3146001B	146Nd	Standard BioTools
CXCR4	12G5	306523	147Sm	BioLegend
CD278/ICOS	C398.4A	3148019B	148Nd	Standard BioTools
CD25	2A3	3149010B	149Sm	Standard BioTools
MIP1β*	D211351	3150004B	150Nd	Standard BioTools
CD107a/LAMP1*	H4A3	3151002B	151Eu	Standard BioTools
TNFα*	Mab11	3152002B	152Sm	Standard BioTools
CD62L/L-selectin	DREG56	3153004B	153Eu	Standard BioTools
CD95	50825	MAB326100	154Sm	R&D
CD279/PD1	EH12.2H7	3155009B	155Gd	Standard BioTools
CD29	TS2/16	3156007B	156Gd	Standard BioTools
CTLA4*	14D3	5012919	157Gd	eBioscience
CD134/OX40	ACT35	3158012B	158Gd	Standard BioTools
CD197/CCR7	G043H7	3159003A	159Tb	Standard BioTools
CD28	CD28.2	3160003B	160Gd	Standard BioTools
Ki-67*	B56	3161007B	161Dy	Standard BioTools
CD69	FN50	3162001B	162Dy	Standard BioTools
IL6*	MQ2-13A5	501115	163Dy	BioLegend
CD45RO	UCHL1	3164007B	164Dy	Standard BioTools
CD127/IL7Ra	A019D5	3165008B	165Ho	Standard BioTools
IL2*	MQ117H12	3166002B	166Er	Standard BioTools
CD27	L128	3167006B	167Er	Standard BioTools
IFNγ*	B27	3168005B	168Er	Standard BioTools
CD45RA	HI100	3169008B	169Tm	Standard BioTools
CD3	UCHT1	3170001B	170Er	Standard BioTools
CD185/CXCR5	RF8B2	3171014B	171Yb	Standard BioTools
CD57	HCD57	3172009B	172Yb	Standard BioTools
Granzyme B*	GB11	3173006B	173Yb	Standard BioTools
CD4	SK3	3174004B	174Yb	Standard BioTools
Perforin*	BD48	3175004B	175Lu	Standard BioTools

Foxp3*	206D	320102	176Yb	BioLegend
TIGIT	MBSA43	3209013B	209Bi	Standard BioTools
IL17*	BL168	512331	89Y	BioLegend
HLA-DR	TU36	Q22158	Qdot(112Cd)	Invitrogen

*Intracellular staining.

Table S3: scRNAseq of differentially expressed genes in LC (n=8) vs. non-LC (n=4) (p<0.05)

Gene	Cluster	Fold-change	Direction*	Adjusted p-value
THEMIS	1 (CD8+ T cells/CTLs)	1.6	up	0.032
NUDT2	1	1.6	up	0.032
PPIE	3 (Monocytes)	1.5	up	0.021

*"up" corresponds to upregulated in LC as compared to non-LC

Table S4: scRNAseq of differentially expressed genes in OR7D2^{high} (n=4) vs. non-LC (n=4) (p<0.05)

Gene	Cluster	Fold-change	Direction*	Adjusted p-value
HIST1H2AM	0 (CD4+ T cells)	2.7	up	0.001
HIST2H2AC	0	1.8	up	0.034
CR1	0	3.4	up	0.034
FGD5-AS1	0	1.4	up	0.034
SVIL	0	1.6	up	0.034
PIP4K2A	0	1.3	up	0.036
NORAD	0	1.4	up	0.036
NUDT2	0	1.6	up	0.038
IFFO2	0	1.5	up	0.039
DENND1B	0	1.3	up	0.039
AC147067.1	0	1.8	up	0.039
RASSF6	0	3.4	up	0.039
ARL15	0	1.3	up	0.039
ARRDC3-AS1	0	1.7	up	0.039
AHNAK	0	1.8	up	0.039
HIST1H2AK	0	2.1	up	0.044
SPCS3	0	1.3	up	0.047
HIST1H2AM	1 (CD8+ T cells/CTLs)	1.6	up	0.004
ITGB1	5 (CD8+ T cells)	1.4	up	0.026

AHNAK	5	8.0	up	0.026
S100A6	5	2.9	up	0.037
HIST1H1E	5	1.8	up	0.037
HIST1H2AM	5	1.7	up	0.037
H1FX	5	1.5	up	0.037
KLF6	5	1.8	up	0.037
MYO1F	5	3.2	up	0.037
TTC39C	5	1.6	up	0.040
IGKV2-24	8 (B cells)	1.7	up	0.011
APOO	0	2.4	down	0.034
MTFP1	0	1.7	down	0.036
AC090360.1	0	1.6	down	0.039
APOO	5	2.1	down	0.026
PECAM1	5	1.6	down	0.037
APOO	7 (CD4+ T cells)	143.1	down	0.027
RGPD2	8 (B cells)	5.1	down	0.002

*"up" corresponds to upregulated in OR7D2^{high} LC as compared to non-LC, "down" corresponds to down-regulated in OR7D2^{high} LC as compared to non-LC

Table S5: scRNAseq of differentially expressed genes in ALAS2^{high} (n=4) vs. non-LC (n=4) (p<0.05)

Gene	Cluster	Fold-change	Direction*	Adjusted p-value
NOTCH2NLB	1 (CD8+ T cells/CTLs)	188.1	up	0.007
PDE3A	1	1.7	up	0.012
THEMIS	1	1.7	up	0.033
IGKV3-11	6 (B cells)	6.6	up	0.019
RMRP	7 (CD4+ T cells)	5.5	up	0.042
IGKV2D-40	8 (B cells)	2.0	up	0.025
ME1	1	3.0	down	0.007
SLC4A10	1	33.6	down	0.033
CXXC5	1	2.5	down	0.040
NOG	5 (CD8+ T cells)	1.8	down	0.046
BACH2	7	3.1	down	0.042
NOG	7	469.8	down	0.042
CLECL1	8	3.8	down	0.025

COPDA1	8	5.2	down	0.038

*"up" corresponds to upregulated in ALAS2^{high} LC as compared to non-LC, "down" corresponds to down-regulated in ALAS2^{high} LC as compared to non-LC

Table S6: T-scan peptides used in study

Peptide	Sequence	Parent protein	Molecular Weight
1	KLWAQCVQL	ORF 1ab	1088.33
2	YLQPRTFLL	S	1150.39
3	LLYDANYFL	ORF 3a	1131.29
4	ALWEIQQVV	ORF 1ab	1085.27
5	LLLDRLNQL	N	1097.32
6	YLFDESGEFKL	ORF 1ab	1347.49
7	FTSDYYQLY	ORF 3a	1199.28
8	TTDPSFLGRY	ORF 1ab	1156.26
9	PTDNYITTY	ORF 1ab	1087.15
10	ATSRTLSYY	M	1061.16
11	NTCDGTTFTY	ORF 1ab	1122.17
12	DTDFVNEFY	ORF 1ab	1149.18
13	GTDLEGNFY	ORF 1ab	1015.04
14	KTFPPTEPK	N	1044.22
15	KCYGVSPTK	S	982.16
16	MVTNNTFTLK	ORF 1ab	1168
17	KTIQPRVEK	ORF 1ab	1098.31
18	KTFPPTEPK	N	1044.22
19	VTDTPKGPK	ORF 1ab	942.08
20	ATEGALNTPK	N	1001.1
21	ASAFFGMSR	N	973.11
22	ATSRTLSYYK	M	1189.33
23	QYIKWPWYI	S	1296.53
24	VYFLQSINF	ORF 3a	1130.31
25	VYIGDPAQL	ORF 1ab	975.11
26	SPRWYFYYL	N	1294.47
27	RPDTRYVL	ORF 1ab	1019.17
28	IPRRNVATL	ORF 1ab	1039.25

N: Nucleoprotein.
M: Membrane protein.
S: Spike protein.
ORF: Open reading frames.

Table S7: Flow cytometry antibodies used in study

1684

Antibody	Clone	Catalog	Fluorochrome	Manufacturer
CD3	UCHT1	11-0038-41	FITC	Invitrogen
CD4	SK3	566356	BV750	BD Biosciences
CXCR4	12G5	17-9999-41	APC	Invitrogen
CXCR5	J252D4	356919	BV421	BioLegend
CCR6	11A9	562724	BV605	BD Biosciences
CD45RO	UCHL1	304227	APC Cy7	BioLegend
live/dead	NA	423107	zombie UV	BioLegend
CD3	UVHT1	612941	BUV496	BD Biosciences
CD8a	RPA-T8	301005	FITC	BioLegend
PD-1	EH12-2H7	329965	BV750	BioLegend
CTLA4*	L3D10	349913	PE-Cy7	BioLegend
IFNγ*	B27	566395	BB700	BD Biosciences
TNFα*	Mab11	502937	BV650	BioLegend
MIP-1β*	D21-1351	562900	BV421	BD Biosciences
live/dead	NA	423105	zombie NIR	BioLegend
CD28	L293	340975	NA	BD Biosciences
CD49d	L25	340976	NA	BD Biosciences

1685 *Intracellular staining.

1686

Figure 1

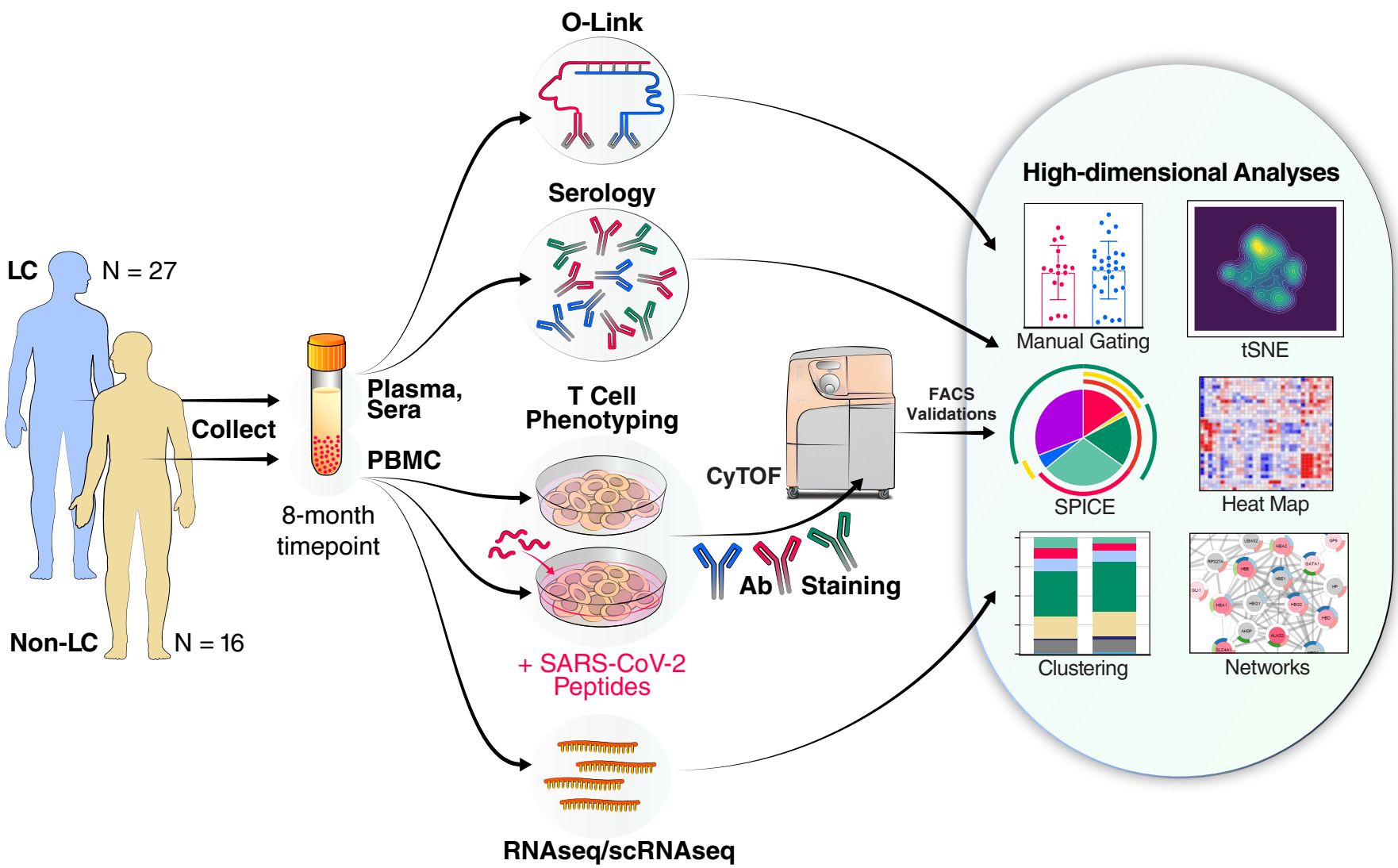
O-Link
Serology
LC
N = 27
Collect
Plasma,
Sera
PBMC
8-month
timepoint
T Cell
Phenotyping
CyTOF
FACS
Validations
Ab
Staining
+ SARS-CoV-2
Peptides
Non-LC
N = 16
RNAseq/scRNAseq
High-dimensional Analyses
Manual Gating
tSNE
SPICE
Heat Map
Clustering
Networks

Figure 2

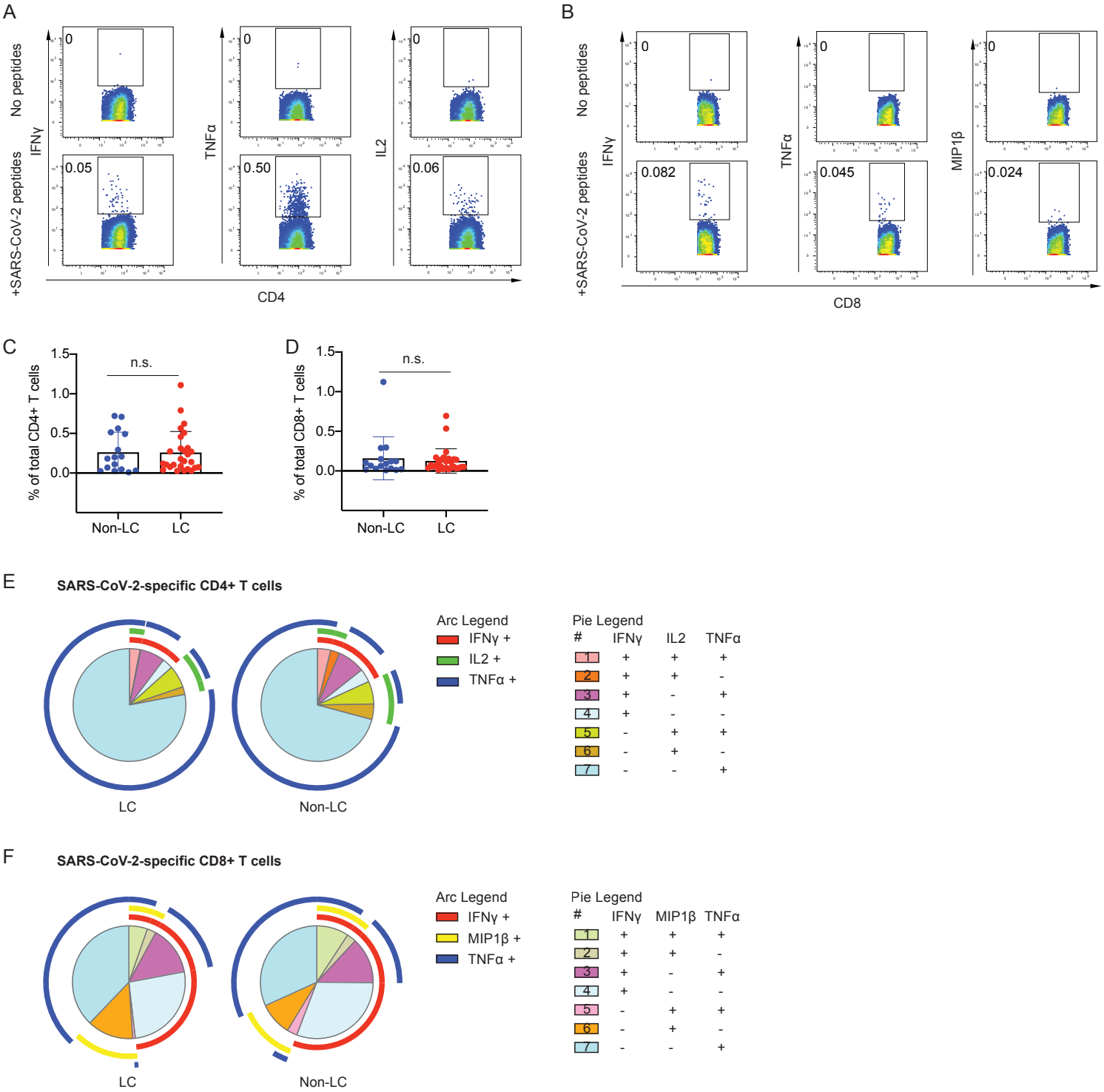
A
No peptides
+SARS-CoV-2 peptides
IFNγ
TNFα
IL2
0
0.05
0.50
0.06
CD4
B
MIP1β
0.082
0.045
0.024
CD8
C
% of total CD4+ T cells
n.s.
Non-LC
LC
D
% of total CD8+ T cells
E
SARS-CoV-2-specific CD4+ T cells
Arc Legend
IFNγ +
IL2 +
TNFα +
Pie Legend
IFNγ IL2 TNFα
1 + + +
2 + + -
3 + - +
4 + - -
5 - + +
6 - + -
7 - - +
F
SARS-CoV-2-specific CD8+ T cells
MIP1β +
IFNγ MIP1β TNFα
1 + + +
2 + + -
3 + - +
4 + - -
5 - + +
6 - + -
7 - - +

Figure 3

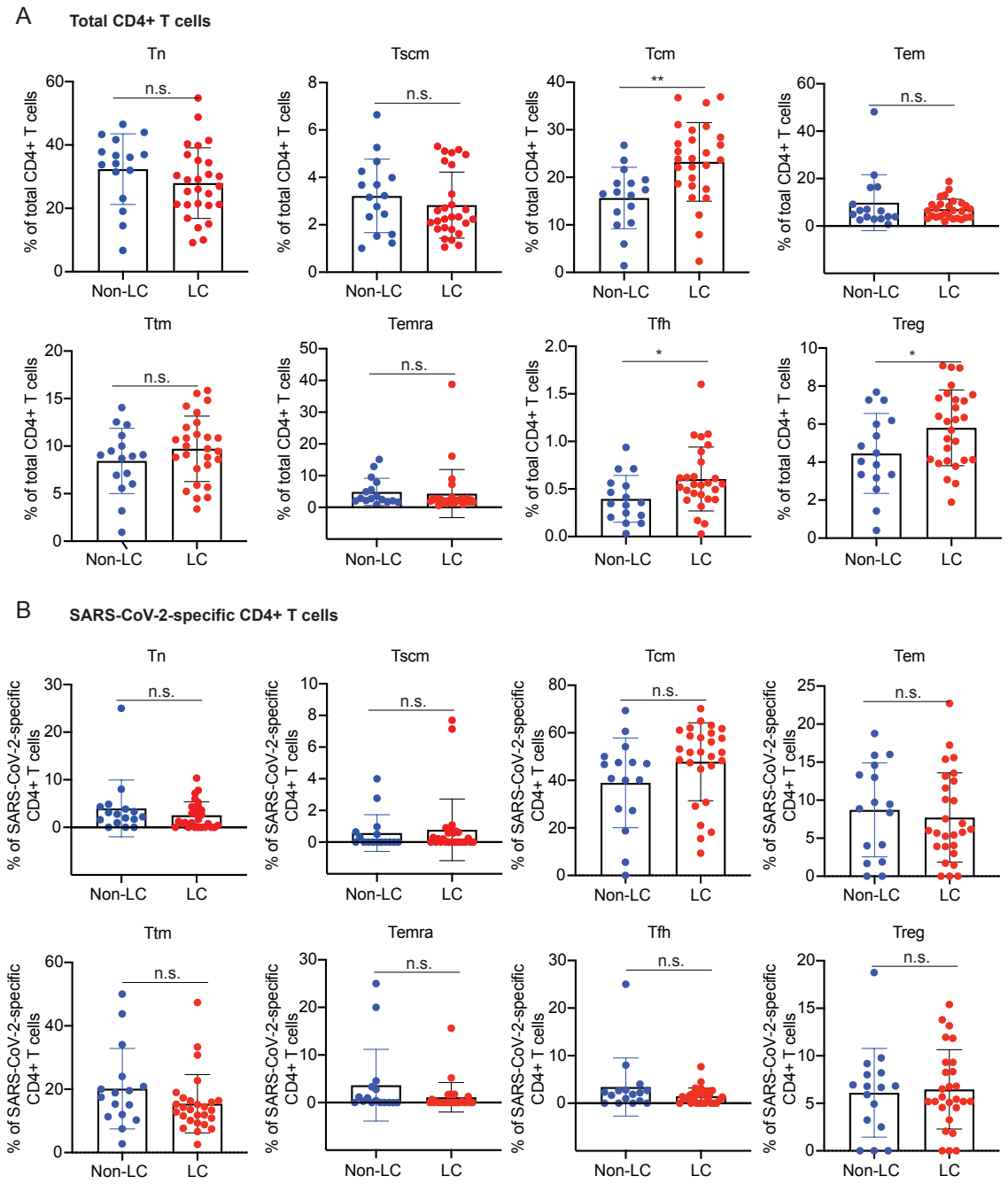
A
Total CD4+ T cells
Tn
Tscm
Tcm
Tem
Ttm
Temra
Tfh
Treg
% of total CD4+ T cells
% of toal CD4+ T cells
n.s.
**
*
Non-LC
LC
B
SARS-CoV-2-specific CD4+ T cells
% of SARS-CoV-2-specific CD4+ T cells

Figure 4

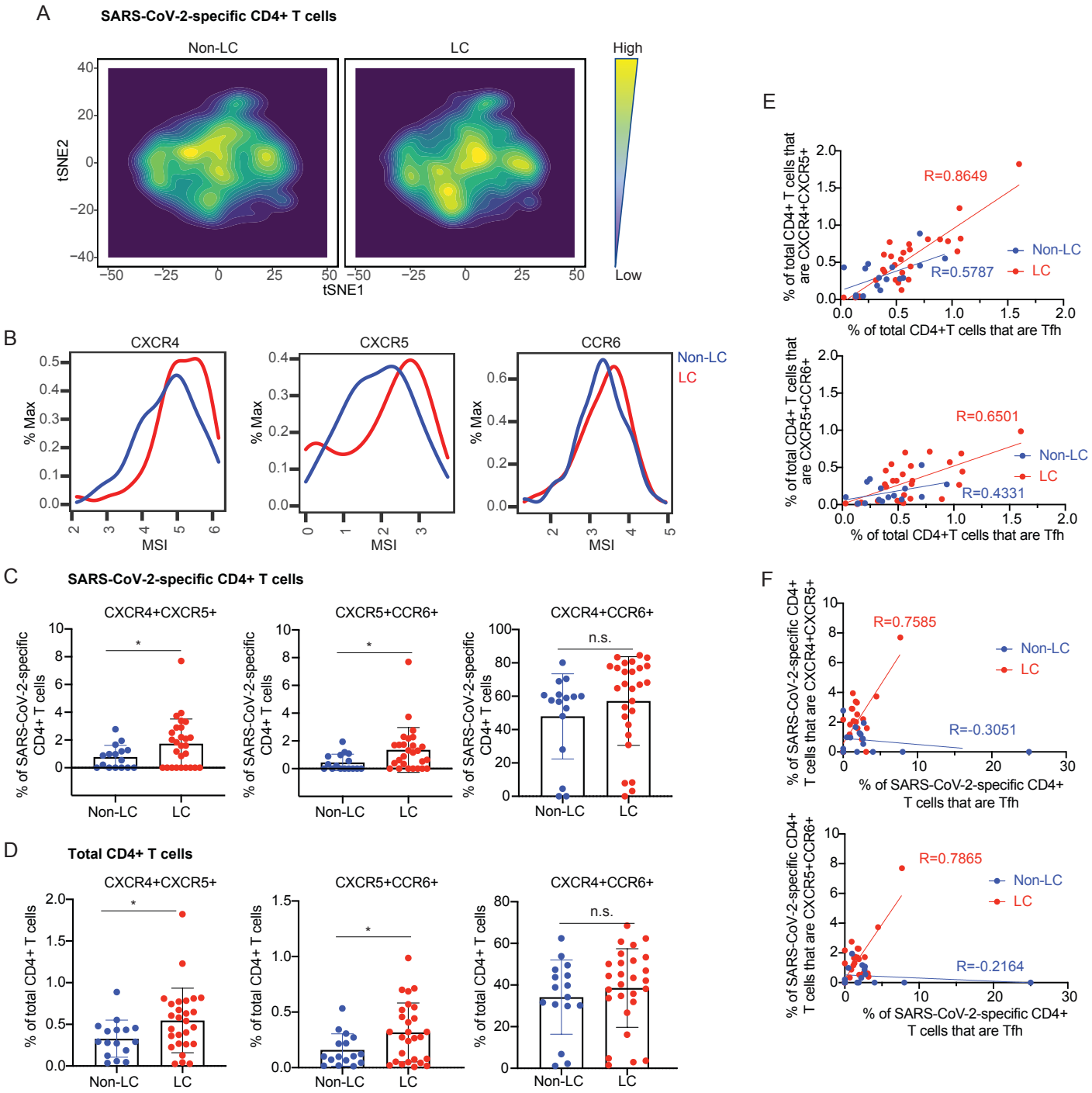
A
SARS-CoV-2-specific CD4+ T cells
Non-LC
LC
High
Low
tSNE2
tSNE1
B
CXCR4
CXCR5
CCR6
% Max
MSI
Non-LC
LC
C
SARS-CoV-2-specific CD4+ T cells
CXCR4+CXCR5+
CXCR5+CCR6+
CXCR4+CCR6+
% of SARS-CoV-2-specific CD4+ T cells
n.s.
D
Total CD4+ T cells
% of total CD4+ T cells
E
% of total CD4+ T cells that are CXCR4+CXCR5+
% of total CD4+T cells that are Tfh
R=0.8649
R=0.5787
% of total CD4+ T cells that are CXCR5+CCR6+
R=0.6501
R=0.4331
F
% of SARS-CoV-2-specific CD4+ T cells that are CXCR4+CXCR5+
% of SARS-CoV-2-specific CD4+ T cells that are Tfh
R=0.7585
R=-0.3051
% of SARS-CoV-2-specific CD4+ T cells that are CXCR5+CCR6+
R=0.7865
R=-0.2164

Figure 5

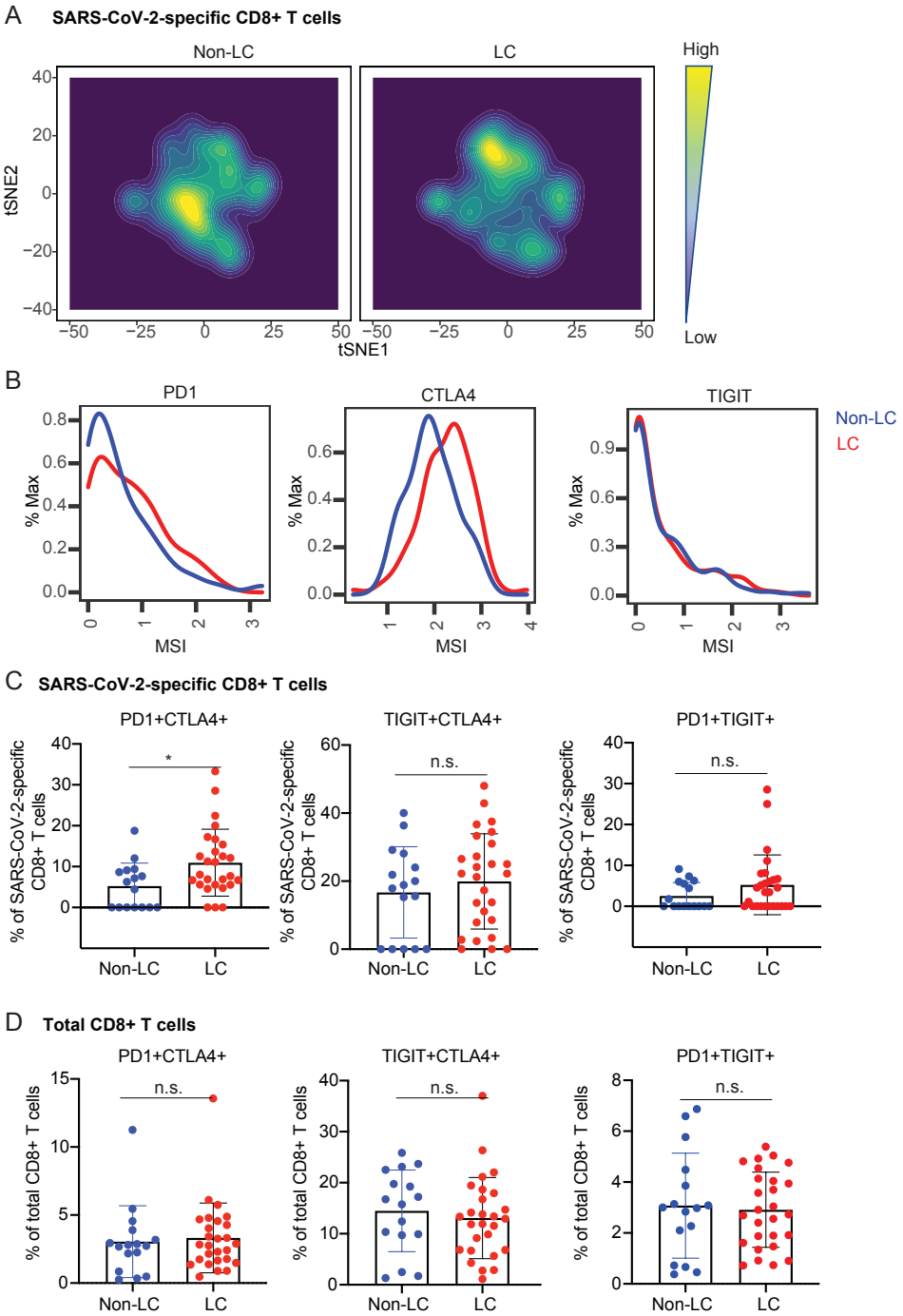
A
SARS-CoV-2-specific CD8+ T cells
Non-LC
LC
High
Low
tSNE2
tSNE1
B
PD1
CTLA4
TIGIT
% Max
MSI
Non-LC
LC
C
SARS-CoV-2-specific CD8+ T cells
PD1+CTLA4+
TIGIT+CTLA4+
PD1+TIGIT+
% of SARS-CoV-2-specific CD8+ T cells
*
n.s.
Non-LC
LC
D
Total CD8+ T cells
% of total CD8+ T cells

Figure 6

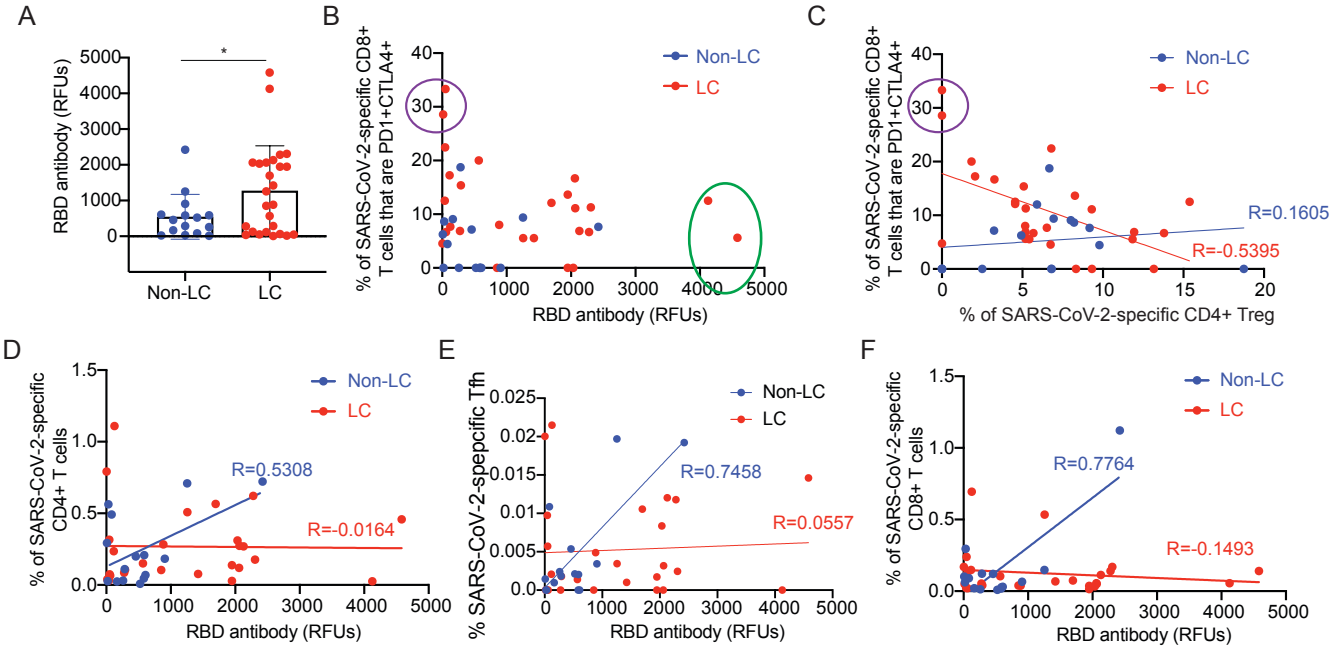
A
RBD antibody (RFUs)
5000
4000
3000
2000
1000
0
*
Non-LC
LC
B
% of SARS-CoV-2-specific CD8+ T cells that are PD1+CTLA4+
40
30
20
10
0
0
1000
2000
3000
4000
5000
RBD antibody (RFUs)
Non-LC
LC
C
% of SARS-CoV-2-specific CD8+ T cells that are PD1+CTLA4+
40
30
20
10
0
0
5
10
15
20
% of SARS-CoV-2-specific CD4+ Treg
Non-LC
LC
R=0.1605
R=-0.5395
D
% of SARS-CoV-2-specific CD4+ T cells
1.5
1.0
0.5
0.0
0
1000
2000
3000
4000
5000
RBD antibody (RFUs)
Non-LC
LC
R=0.5308
R=-0.0164
E
% SARS-CoV-2-spepcific Tfh
0.025
0.02
0.015
0.01
0.005
0.0
0
1000
2000
3000
4000
5000
RBD antibody (RFUs)
Non-LC
LC
R=0.7458
R=0.0557
F
% of SARS-CoV-2-specific CD8+ T cells
1.5
1.0
0.5
0.0
0
1000
2000
3000
4000
5000
RBD antibody (RFUs)
Non-LC
LC
R=0.7764
R=-0.1493

Figure 7

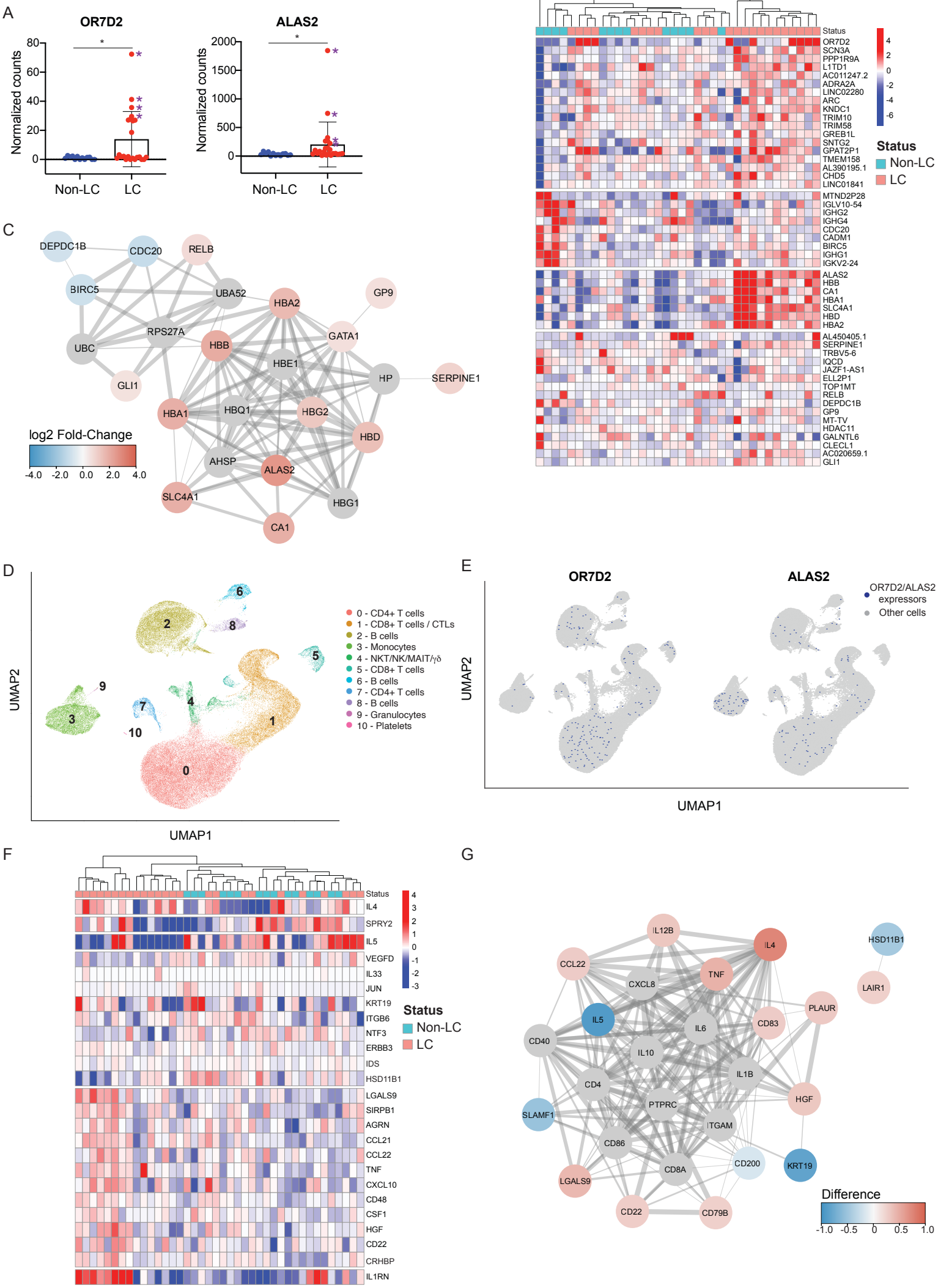
A
OR7D2
ALAS2
Normalized counts
Non-LC
LC
B
Status
Non-LC
LC
C
log2 Fold-Change
-4.0 -2.0 0.0 2.0 4.0
D
UMAP1
UMAP2
0 - CD4+ T cells
1 - CD8+ T cells / CTLs
2 - B cells
3 - Monocytes
4 - NKT/NK/MAIT/γδ
5 - CD8+ T cells
6 - B cells
7 - CD4+ T cells
8 - B cells
9 - Granulocytes
10 - Platelets
E
OR7D2/ALAS2 expressors
Other cells
F
G
Difference
-1.0 -0.5 0 0.5 1.0